

Markus Wolff, Yufei Cao, Bernd Flemisch, Rainer Helmig and
Barbara Wohlmuth

Multipoint flux approximation L-method in 3D: numerical convergence and application to two-phase flow through porous media

Abstract: We thoroughly investigate the multipoint flux approximation L-method in 3D and apply this method to several realistic two-phase flow problems. Detailed transmissibility matrices for the flux calculation are presented, a novel selecting criterion for proper L-stencils is proposed, and a simple boundary handling approach is suggested. We further study the numerical convergence of the L-method through two FVCA6 benchmark tests on highly skewed and nonplanar grids. The results show that the new criterion is very robust for challenging cases and the boundary treatment is sufficiently accurate. The simulations for the advection-dominated Buckley–Leverett problem and the capillary-diffusion-dominated McWhorter problem exhibit the superiority of the L-method over two-point flux approximation on general non-K-orthogonal grids. For complex porous media flow in natural geological formations, the efficiency of the numerical method is crucial. Thus, local grid adaptivity using a refinement indicator is presented and applied to two infiltration scenarios which illustrate the performance of the L-method for complex physical processes (capillary pressure, gravity, etc.) and heterogeneity/anisotropy.

Keywords: Multipoint Flux, L-Method, Three Dimensions, Numerical Convergence, Local Grid Refinement, Refinement Indicator, Two-Phase Flow, Anisotropy, Heterogeneity.

Mathematics Subject Classifications 2010: 65M08, 76S05, 76M12

Markus Wolff: University of Stuttgart, Department of Hydromechanics and Modeling of
Hydroystems, Stuttgart, Germany, Markus.Wolff@iws.uni-stuttgart.de

Yufei Cao: University of Stuttgart, Department of Hydromechanics and Modeling of Hydroystems,
Stuttgart, Germany, Yufei.Cao@iws.uni-stuttgart.de

Bernd Flemisch: University of Stuttgart, Department of Hydromechanics and Modeling of
Hydroystems, Stuttgart, Germany, Bernd.Flemisch@iws.uni-stuttgart.de

Rainer Helmig: University of Stuttgart, Department of Hydromechanics and Modeling of
Hydroystems, Stuttgart, Germany, Rainer.Helmig@iws.uni-stuttgart.de

Barbara Wohlmuth: Technical University of Munich, Centre for Mathematical Sciences, Garching,
Germany, barbara.wohlmuth@ma.tum.de

The authors would like to thank the German Research Foundation (DFG) for financial support of the projects within the Cluster of Excellence in Simulation Technology (EXC 310/1) at the University of Stuttgart and the International Research Training Group “Nonlinearities and Upscaling in Porous Media” (GRK 1398/2).

Contract/grant sponsor: DFG; contract/grant number: GRK 1398/2; EXC 310/1.

1 Introduction

Cell-centered finite volume techniques are quite popular in reservoir simulation to solve the elliptic flow equation. A physically intuitive control volume formulation is the so-called two-point flux approximation (TPFA) which is widely used due to its simplicity and efficiency. However, it is consistent if and only if the simulation grids are K-orthogonal [29]. For general non-K-orthogonal grids, the TPFA does not work properly due to the $\mathcal{O}(1)$ error in its solution [3, 50]. Mesh refinement cannot reduce the error as long as it does not improve the K-orthogonality of the grid. This was one of the prime motivations for the independent development of multipoint flux approximations (MPFA) from the research group of Aavatsmark et al. [4] and full-tensor flux continuous schemes from the research group of Edwards et al. [21]. Both methods are similar, but differ in the choices of geometrical points and control volumes. The extension from TPFA to MPFA gives a correct discretization of flow equations for general grids and anisotropic permeability tensors.

There are many variants of the MPFA method, like the $\mathcal{O}(\eta)$ -method [20, 41], the L-method [9], the U-method [6], the Z-method [39], the enriched MPFA method [18], or the nine point scheme of [45]. The most popular is the $\mathcal{O}(0)$ -method, often simply called the O-method. A class of MPFA O-methods can be found in [2] for quadrilaterals, in [5, 34] for hexahedral grids and in [26] for general three-dimensional unstructured meshes. The convergence of the family of O-methods is tested and discussed in [7, 8, 23, 41] by presenting numerical convergence results and in [11, 32, 33, 48] by giving theoretical proofs. The M-matrix monotonicity of the MPFA methods is discussed in [22, 37, 38]. It is an important property for multiphase flow to avoid unphysical oscillations in the discrete solution.

In this chapter, the MPFA L-method is investigated. It has some advantages compared to the O-variant. The flux stencils are smaller, the domain of convergence as well as the domain of monotonicity is larger and the treatment of hanging nodes and thus the capability for local adaptivity is naturally included. The first introduction of the L-method is given in Aavatsmark et al. [9] for quadrilateral grids in two dimensions. Aavatsmark et al. [10] further extend it to three dimensions. An alternative but closely related scheme with anisotropy-favoring triangulation is presented in Pal and Edwards [40]. Mundal et al. [36] have tested the L-method for different heterogeneous, highly anisotropic, elliptic problems from the FVCA5 benchmark on triangular and quadrilateral grids. The boundary influence on the convergence rate and the geometrical interpretation of the original transmissibility-based criterion in the case of homogeneous media are studied in Cao et al. [16]. The first theoretical convergence proof of the L-method with homogeneous media on uniform grids is given in Cao et al. [17] through the equivalence to a modified conforming finite element method. Stephansen [46] further investigates the convergence on general grids by linking the L-method to mimetic finite differences (MFD) [14].

In this chapter, the numerical convergence of the L-method in 3D is studied by comparing with the TPFA and the MFD method. Further, it is applied to two-phase flow in porous media and tested and validated on standard benchmark problems as well as on more realistic test scenarios. For solving the nonlinear coupled two-phase flow equations, the numerical method has to be efficient. Thus, we introduce mesh adaptivity with hanging nodes in combination with the MPFA L-method. In contrast to the O-method, the L-method naturally allows for hanging nodes and thus is quite attractive in the case of adaptive mesh refinement.

This chapter is organized as follows. In Section 2, the implementation of the MPFA L-method in 3D is illustrated in detail. The standard criterion for choosing a proper L-stencil for flux calculation is discussed, and a new more robust criterion is proposed. Moreover, a simplified boundary handling approach is presented. Section 3 thoroughly investigates the numerical convergence of the L-method through two benchmark examples, where convergence rates of pressure and normal velocity are studied. Additionally, the different selection criteria of the L-stencil are tested and the MPFA method is compared to the TPFA and MFD methods. Details for the use of nonconforming, adaptive grids with the L-method are given in Section 4, where the focus is on different types of interaction volumes around hanging nodes and boundary treatment. In Section 5, the L-method is applied to four typical two-phase flow problems addressing different physical regimes like the advection-dominated case, the capillary-diffusion-dominated case or the capillary pressure/gravity-dominated case as well as homogeneous, heterogeneous, and anisotropic porous media. The 3D MPFA L-method is implemented in the simulation toolbox DuMu^x [24], which is based on the DUNE framework [13]. For the convergence study the sparse direct solver PARDISO [43, 44] is used as linear solver.

2 The MPFA L-method in 3D

In this section, the MPFA L-scheme is introduced for the second-order elliptic equation

$$-\nabla \cdot (\mathbf{K} \nabla p) = q, \quad \text{in } \Omega \subset \mathbb{R}^3, \quad (2.1)$$

where Ω is the bounded Lipschitz domain of interest, $\mathbf{K} : \Omega \rightarrow \mathbb{R}^{3 \times 3}$ is a symmetric and uniformly positive definite permeability tensor, p is the pressure and q is the source term. Different from [10], the detailed geometrical information for four L-stencils of each subinterface and their transmissibility matrices are described and given here. Additionally to the L-shape selection criterion given in [10], we introduce a new transmissibility-based criterion which is supposed to be robust also for very challenging grids. A simple but sufficiently accurate treatment of fluxes through each subinterface connecting to or lying on the boundary is introduced. This allows an easy implementation of more complex domain shapes and boundary configurations (especially in 3D) and thus provides the possibility to apply the method to realistic scenarios.

2.1 Details of the scheme

Let \mathcal{T}_h be a hexahedral partition of the domain Ω . The principle of the control volume formulation is the local mass conservation of equation (2.1) over each grid cell $K \in \mathcal{T}_h$ (the so-called control volume)

$$-\int_{\partial K} \mathbf{K} \nabla p \cdot \mathbf{n} \, ds = \int_K q \, dx, \quad (2.2)$$

where ∂K is the boundary of the cell K which is the union of six cell faces e_i , $i = 1, \dots, 6$ (Figure 2.1), and \mathbf{n} is the unit outer normal vector on ∂K . If the numerical approximation of the flux $-\int_{e_i} \mathbf{K} \nabla p \cdot \mathbf{n} \, ds$ through each cell face e_i is denoted as f^i , then the local control volume formulation (2.2) can be written as

$$\sum_{i=1}^6 f^i = \int_K q \, dx. \quad (2.3)$$

Various developments of the numerical fluxes f^i lead to different cell-centered finite volume schemes. The TPFA method, for example, approximates the flux f^1 in Figure 2.1 as a whole using the information of the two neighboring cells of face e_1 . In contrast, the L-method calculates f^1 as the sum of the fluxes through four subinterfaces as $f^1 = \sum_{j=1}^4 f_j^1$, using the geometry and soil matrix properties of multiple grid cells.

In case of 3D, there are four possible L-stencils instead of two choices in 2D to calculate the numerical flux through each subinterface inside the domain, and each L-stencil contains four interacting cells instead of three for 2D cases. Figure 2.2 shows the four possibilities corresponding to the subinterface $\bar{x}_1 \bar{x}_4 \bar{x}_0 \bar{x}_5$, where (a) and (b) are centered L-stencils which have a center cell interacting with the other three cells, and (c) and (d) are named noncentered L-stencils [10]. In the following, the flux calculation through the subinterface $\bar{x}_1 \bar{x}_4 \bar{x}_0 \bar{x}_5$ is described in detail.

For each subvolume, e.g. $x_1 \bar{x}_1 \bar{x}_4 \bar{x}_2 \bar{x}_3 \bar{x}_5 \bar{x}_0 \bar{x}_6$ in the L-stencil (a), a linear pressure is applied which leads to 16 degrees of freedom for the whole L-stencil. Thus,

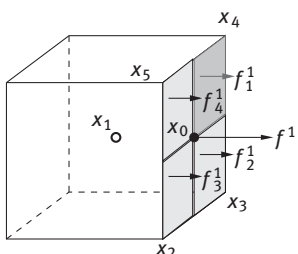


Figure 2.1: Control volume K and its face fluxes.

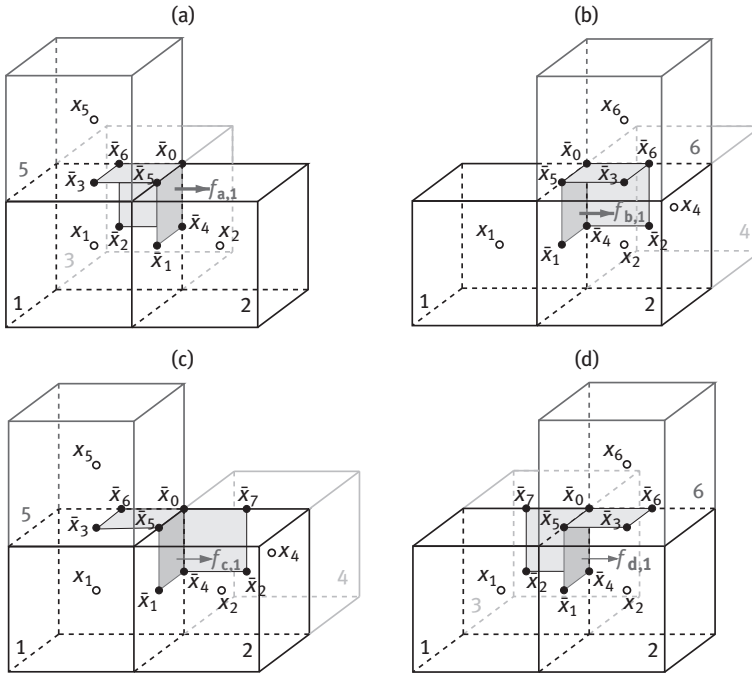


Figure 2.2: Four L-stencils for the flux calculation through subinterface $\bar{x}_1\bar{x}_4\bar{x}_0\bar{x}_5$.

16 equations for determining the unknown coefficients $\alpha_{0j}, \alpha_{1j}, \alpha_{2j}, \alpha_{3j}$ of the four affine pressure functions $p_j^f(\mathbf{x}) = \alpha_{0j} + \alpha_{1j}x + \alpha_{2j}y + \alpha_{3j}z, j = 1, 2, 3, 5$, in the four tetrahedra $\bar{x}_1\bar{x}_2\bar{x}_3x_1$, $\bar{x}_1\bar{x}_4\bar{x}_5x_2$, $\bar{x}_2\bar{x}_4\bar{x}_6x_3$, and $\bar{x}_3\bar{x}_5\bar{x}_6x_5$ are required, see Figure 2.2. Here, $\mathbf{x} = (x, y, z)^T$ represents the coordinate vector of an arbitrary point in 3D Eulerian space. The tetrahedra used to construct the linear affine functions and their constant gradients are listed in Table 2.1 for the four kinds of L-stencils (a)–(d). To close the numerical scheme, the physically meaningful conditions in Table 2.2 are forced to be satisfied for each L-stencil.

Denote the fluxes through the three subinterfaces $\bar{x}_1\bar{x}_4\bar{x}_0\bar{x}_5$, $\bar{x}_2\bar{x}_4\bar{x}_0\bar{x}_6$, and $\bar{x}_3\bar{x}_5\bar{x}_0\bar{x}_6$ inside the L-stencil (a) as $f_{a,1}, f_{a,2}, f_{a,3}$, then a small local algebraic system for the flux vector $\mathbf{f}_a = (f_{a,1}, f_{a,2}, f_{a,3})^T = \mathbf{T}_a \mathbf{u}_a$ can be derived by using the aforementioned constraints. Here, \mathbf{T}_a is the so-called transmissibility matrix, and $\mathbf{u}_a = (p_1, p_2, p_3, p_5)^T$ is the local pressure (solution) vector for the L-stencil (a), where p_j is the function value of $p_j^f(\mathbf{x})$ at the cell center $x_j, j = 1, 2, 3, 5$. For completeness, the calculation of \mathbf{T}_a for the L-stencil (a) will be described below in detail (see also [10]). Due to the similarity, the derivation of the transmissibility matrices $\mathbf{T}_b, \mathbf{T}_c, \mathbf{T}_d$ are omitted but the matrix forms are given in the appendix.

Table 2.1: The two tetrahedra used to calculate the flux through each of the three subinterfaces for the four L-stencils (a)–(d), see Figure 2.2.

L-stencil \ Subinterface	$\bar{x}_1\bar{x}_4\bar{x}_0\bar{x}_5$	$\bar{x}_2\bar{x}_4\bar{x}_0\bar{x}_6$	$\bar{x}_3\bar{x}_5\bar{x}_0\bar{x}_6$
(a)	$\bar{x}_1\bar{x}_2\bar{x}_3x_1$	$\bar{x}_1\bar{x}_2\bar{x}_3x_1$	$\bar{x}_1\bar{x}_2\bar{x}_3x_1$
	$\bar{x}_1\bar{x}_4\bar{x}_5x_2$	$\bar{x}_2\bar{x}_4\bar{x}_6x_3$	$\bar{x}_3\bar{x}_5\bar{x}_6x_5$
(b)	$\bar{x}_1\bar{x}_4\bar{x}_5x_1$	$\bar{x}_1\bar{x}_2\bar{x}_3x_2$	$\bar{x}_1\bar{x}_2\bar{x}_3x_2$
	$\bar{x}_1\bar{x}_2\bar{x}_3x_2$	$\bar{x}_2\bar{x}_4\bar{x}_6x_4$	$\bar{x}_3\bar{x}_5\bar{x}_6x_6$
L-stencil \ Subinterface	$\bar{x}_1\bar{x}_4\bar{x}_0\bar{x}_5$	$\bar{x}_2\bar{x}_4\bar{x}_0\bar{x}_7$	$\bar{x}_3\bar{x}_5\bar{x}_0\bar{x}_6$
(c)	$\bar{x}_1\bar{x}_3\bar{x}_4x_1$	$\bar{x}_1\bar{x}_2\bar{x}_5x_2$	$\bar{x}_1\bar{x}_3\bar{x}_4x_1$
	$\bar{x}_1\bar{x}_2\bar{x}_5x_2$	$\bar{x}_2\bar{x}_4\bar{x}_7x_4$	$\bar{x}_3\bar{x}_5\bar{x}_6x_5$
(d)	$\bar{x}_1\bar{x}_2\bar{x}_5x_1$	$\bar{x}_1\bar{x}_2\bar{x}_5x_1$	$\bar{x}_1\bar{x}_3\bar{x}_4x_2$
	$\bar{x}_1\bar{x}_3\bar{x}_4x_2$	$\bar{x}_2\bar{x}_4\bar{x}_7x_3$	$\bar{x}_3\bar{x}_5\bar{x}_6x_6$

Table 2.2: Required constraints for constructing the MPFA L-scheme in 3D.

	Conditions/ Degrees of freedom	Number	Total equations
Each subinterface ($\times 3$)	Flux continuity	1	16
	Full pressure continuity	3	
Each interacting cell ($\times 4$)	Pressure	1	

By applying the three flux continuity conditions, we get

$$\begin{aligned} f_{a,1} &= -\mathbf{n}_1^T \mathbf{K}_1 \nabla p_1 = -\mathbf{n}_1^T \mathbf{K}_2 \nabla p_2, \\ f_{a,2} &= -\mathbf{n}_2^T \mathbf{K}_1 \nabla p_1 = -\mathbf{n}_2^T \mathbf{K}_3 \nabla p_3, \\ f_{a,3} &= -\mathbf{n}_3^T \mathbf{K}_1 \nabla p_1 = -\mathbf{n}_3^T \mathbf{K}_5 \nabla p_5, \end{aligned} \quad (2.4)$$

where \mathbf{n}_i , $i = 1, 2, 3$, are the normal vectors of the three subinterfaces having the length equal to the subinterface area, and \mathbf{K}_j , $j = 1, 2, 3, 5$, are the permeabilities of the four interacting cells. Using the tetrahedra given in Table 2.1, the pressure gradient on the interacting cell j can be expressed as

$$\nabla p_j = \frac{1}{T_j} \sum_{k=1}^3 \mathbf{v}_{jk} (\bar{p}_{jk} - p_j), \quad j = 1, 2, 3, 5, \quad (2.5)$$

where \bar{p}_{jk} is the pressure value at the continuity point \bar{x}_{jk} , and \mathbf{v}_{jk} is the inward normal vector to the tetrahedron face opposite to \bar{x}_{jk} . The length of \mathbf{v}_{jk} is equal to

twice the area of the face to which it is normal. This face area can be easily expressed as cross product of the two vectors that span the tetrahedron face. The coefficient T_j is given by the triple product of the three vectors that span the tetrahedron and is equal to six times the volume of the tetrahedron. For more details on \mathbf{v}_{jk} and T_j , see [2]. In particular for the L-stencil (a), we have

$$\begin{aligned}\bar{p}_{11} &= \bar{p}_1, & \bar{p}_{12} &= \bar{p}_2, & \bar{p}_{13} &= \bar{p}_3, \\ \bar{p}_{21} &= \bar{p}_4, & \bar{p}_{22} &= \bar{p}_1, & \bar{p}_{23} &= \bar{p}_5, \\ \bar{p}_{31} &= \bar{p}_2, & \bar{p}_{32} &= \bar{p}_4, & \bar{p}_{33} &= \bar{p}_6, \\ \bar{p}_{51} &= \bar{p}_6, & \bar{p}_{52} &= \bar{p}_5, & \bar{p}_{53} &= \bar{p}_3.\end{aligned}$$

As done in [10], we further eliminate the additional unknowns \bar{p}_{3+i} , $i = 1, 2, 3$ at the edge centers by using the linear pressure variation of the interacting cell 1. Let $\mathbf{r}_i = \bar{\mathbf{x}}_{3+i} - \mathbf{x}_1$, $i = 1, 2, 3$, and $r_{1ki} = \mathbf{v}_{1k}^T \mathbf{r}_i / T_1$, $i, k = 1, 2, 3$. Inserting these expressions into equation (2.5) we obtain

$$\bar{p}_{3+i} = \nabla p_1 \cdot (\bar{\mathbf{x}}_{3+i} - \mathbf{x}_1) + p_1 = \sum_{k=1}^3 r_{1ki}(\bar{p}_{1k} - p_1) + p_1, \quad i = 1, 2, 3, \quad (2.6)$$

where $\mathbf{x}_1, \bar{\mathbf{x}}_{3+i}$ are the coordinate vectors of points x_1 and \bar{x}_{3+i} .

From equations (2.4) to (2.6), it is easy to see that the flux through each subinterface of the L-stencil (a) can be spanned by the pressures at the points \bar{x}_i , $i = 1, 2, 3$, and the cell centers x_j , $j = 1, 2, 3, 5$. The first equality in equation (2.4) gives the matrix expression of the flux vector across the three subinterfaces as

$$\mathbf{f}_a = \mathbf{C}\mathbf{v}_a + \mathbf{D}\mathbf{u}_a, \quad \mathbf{C} \in \mathcal{R}^{3 \times 3}, \quad \mathbf{D} \in \mathcal{R}^{3 \times 4}, \quad (2.7)$$

where $\mathbf{v}_a = (\bar{p}_1, \bar{p}_2, \bar{p}_3)^T$ is the pressure vector of pressure continuity points \bar{x}_1, \bar{x}_2 and \bar{x}_3 . After introducing the quantity $\omega_{ijk} = \mathbf{n}_i^T \mathbf{K}_j \mathbf{v}_{jk} / T_j$, the matrices can be written as

$$\mathbf{C} = \begin{pmatrix} -\omega_{111} & -\omega_{112} & -\omega_{113} \\ -\omega_{211} & -\omega_{212} & -\omega_{213} \\ -\omega_{311} & -\omega_{312} & -\omega_{313} \end{pmatrix}, \quad \mathbf{D} = \begin{pmatrix} \omega_{111} + \omega_{112} + \omega_{113} & 0 & 0 & 0 \\ \omega_{211} + \omega_{212} + \omega_{213} & 0 & 0 & 0 \\ \omega_{311} + \omega_{312} + \omega_{313} & 0 & 0 & 0 \end{pmatrix}.$$

Furthermore, an algebraic system of the form

$$\mathbf{A}\mathbf{v}_a = \mathbf{B}\mathbf{u}_a, \quad \mathbf{A} \in \mathcal{R}^{3 \times 3}, \quad \mathbf{B} \in \mathcal{R}^{3 \times 4} \quad (2.8)$$

can be derived from the second equality of the flux continuity equations (2.4), with

$$\mathbf{A} = \begin{pmatrix} \omega_{111} - \omega_{122} - & \omega_{112} - \omega_{121}r_{121} - & \omega_{113} - \omega_{121}r_{131} - \\ \omega_{121}r_{111} - \omega_{123}r_{112} & \omega_{123}r_{122} & \omega_{123}r_{132} \\ \omega_{211} - \omega_{232}r_{111} - & \omega_{212} - \omega_{231} - & \omega_{213} - \omega_{232}r_{131} - \\ \omega_{233}r_{113} & \omega_{232}r_{121} - \omega_{233}r_{123} & \omega_{233}r_{133} \\ \omega_{311} - \omega_{351}r_{113} - & \omega_{312} - \omega_{351}r_{123} - & \omega_{313} - \omega_{353} - \\ \omega_{352}r_{112} & \omega_{352}r_{122} & \omega_{351}r_{133} - \omega_{352}r_{132} \end{pmatrix},$$

$$\mathbf{B} = \begin{pmatrix} \omega_{111} + \omega_{112} + \omega_{113} + & -(\omega_{121} +) & 0 & 0 \\ \omega_{121}(1 - r_{111} - r_{121} - r_{131}) + & \omega_{122} + \omega_{123} & & \\ \omega_{123}(1 - r_{112} - r_{122} - r_{132}) & & & \\ \omega_{211} + \omega_{212} + \omega_{213} + & 0 & -(\omega_{231} +) & 0 \\ \omega_{232}(1 - r_{111} - r_{121} - r_{131}) + & & \omega_{232} + \omega_{233} & \\ \omega_{233}(1 - r_{113} - r_{123} - r_{133}) & & & \\ \omega_{311} + \omega_{312} + \omega_{313} + & 0 & 0 & -(\omega_{351} +) \\ \omega_{351}(1 - r_{113} - r_{123} - r_{133}) + & & & \omega_{352} + \omega_{353} \end{pmatrix}.$$

Finally, the transmissibility matrix \mathbf{T}_a for the L-stencil (a) is obtained as

$$\mathbf{T}_a = \mathbf{C}\mathbf{A}^{-1}\mathbf{B} + \mathbf{D} \in \mathcal{R}^{3 \times 4}, \quad (2.9)$$

provided that the matrix \mathbf{A} is nonsingular. Monotonicity of the method ensures that the matrix \mathbf{A} is regular. The monotonicity of 2D MPFA methods is discussed in [9, 38], for 3D this is still a topic of ongoing research.

2.2 Criterion for choosing the proper L-stencil

The choice of a proper L-stencil for each subinterface is crucial for the robustness of the L-method. In this context, we define a method to be robust, if it provides physically meaningful solutions with an acceptable magnitude of error and for a wide spectrum of applications. As the selection of one of the four cases (Figure 2.2) has to be made a priori, an appropriate criterion is needed. In [10, 36] the sign property of the transmissibility coefficients of a L-stencil is identified to be an important criterion. Considering a certain flux face on a regular grid the idea is that all transmissibility coefficients of cells located at one side of this flux face should have the same sign, leading to fluxes in the same direction, while all transmissibility coefficients on the other side should have the opposite sign. Therefore, [10] proposes to choose the L-stencil with the smallest s_l value, where

$$s_l = |\mathbf{T}_{l,11} - \mathbf{T}_{l,12}|. \quad (2.10)$$

The capital index $l = a, b, c, d$ denotes the type of the L-stencil, $\mathbf{T}_{l,1i}$ are the transmissibility coefficients of cell i for flux subinterface 1 ($\tilde{x}_1\tilde{x}_4\tilde{x}_0\tilde{x}_5$). In [10] the authors show that for parallelepiped grids the s_l -criterion always yields a robust L-stencil.

However, for irregular grids, which are not close to K-orthogonal grids, a good choice of the L-stencil is more difficult. For grids with large skewness, none of the transmissibilities of the four L-cases might fulfill the sign criterion. Especially in the 3D case, it is not obvious if the smallest s_i value also leads to the most robust stencil (see Section 3). Thus, a new criterion is developed from the following ideas: (1) in the K-orthogonal case the chosen transmissibility should satisfy the sign property; (2) it should include more than the two neighboring cells at the respective flux subinterface to better cover the 3D behavior; (3) it should lead to a unique flux stencil for the cases in which the sign property cannot give a unique choice. We propose to choose the L-stencil with the largest \bar{t}_i value, where

$$\begin{aligned}\bar{t}_a &= |T_{a,11} + T_{a,13} + T_{a,15}|, \\ \bar{t}_b &= |T_{b,12} + T_{b,14} + T_{b,16}|, \\ \bar{t}_c &= |T_{c,11} + T_{c,15}|, \\ \bar{t}_d &= |T_{d,11} + T_{d,13}|.\end{aligned}\tag{2.11}$$

On one hand the $T_{l,1i}$ in equation (2.11) tend to have the same sign if the absolute of their sum is larger. Thus, it is more likely that the chosen transmissibility shows the expected sign property. On the other hand the transmissibility that has the largest impact on the flux through subinterface $\tilde{x}_1\tilde{x}_4\tilde{x}_0\tilde{x}_5$ is always preferred. This is in line with one of the basic ideas of the L-method, namely to choose the flux stencil according to the preferred direction of flow. If the contributing cells lead to higher fluxes through a subinterface, the orientation of the L-shape most likely is in better agreement with the direction of the streamlines. This leads to a consistent choice of the L-stencils even in the case of irregular grids with large skewness and thus increases the robustness of the MPFA L-method (see Section 3.1). However, it is not obvious which criterion yields more accurate results. In our numerical examples, the new criterion is more robust.

2.3 Boundary handling

In Aavatsmark et al. [9], the boundary handling of the L-method in 2D is shortly mentioned where the concept of ghost cells is proposed. Especially, the flux through the second half edge near the boundary is difficult to derive in a consistent way and therefore the O-method is suggested. Cao et al. [16] further studies the influence of different boundary treatments using the O-method on the convergence rate. Instead of ghost cells or the O-method, we combine the TPFA discretization with the concept of weighting factors to handle the boundary region. Although this method is rather simple, it is still sufficiently accurate for many applications.

As seen from Figure 2.3, there are three boundary situations we need to take into account. In case (a) the cell face $x_2x_3x_4x_5$ lies on the boundary, so it is straightfor-

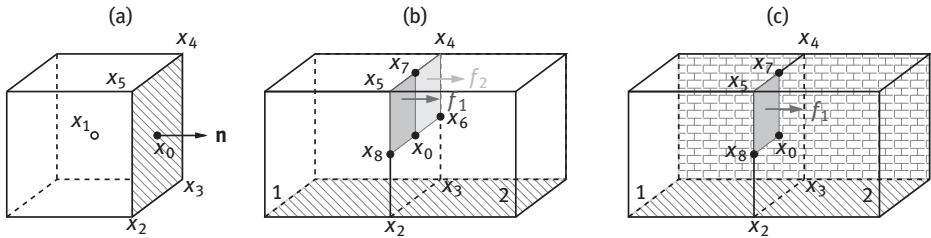


Figure 2.3: Boundary handling of three cases: the flux calculation through the cell face $x_2x_3x_4x_5$ (a) on the boundary, (b) intersecting with one boundary face, (c) intersecting with two boundary faces.

ward for the Neumann conditions to get the flux. For the Dirichlet boundary, a two-point approximation

$$f_{\text{TPFA}} = -\frac{|\mathbf{K}^T \mathbf{n}|}{|x_0 - x_1|} (p_0 - p_1) |s| \quad (2.12)$$

is used, where \mathbf{n} is the unit outer normal vector of the cell face, $|\mathbf{K}^T \mathbf{n}|$ is the norm of the face permeability vector $\mathbf{K}^T \mathbf{n}$, p_0 and p_1 are the pressures at the face center x_0 and the cell center x_1 , respectively, $|x_0 - x_1|$ is the distance between the two centers, and $|s|$ is the area of the cell face. This discretization is exact for K-orthogonal grids, and its impact on the convergence of the whole domain is very small for non-K-orthogonal grids (see Section 3).

Case (b) consider the cell face intersecting with one boundary face, where the flux f_1 through the subinterface $x_0x_7x_5x_8$ and the flux f_2 through the subinterface $x_0x_6x_4x_7$ can be, respectively, obtained from two separate inner interaction volumes using the L-method introduced in Section 2.1. Then the flux f through the whole cell face $x_2x_3x_4x_5$ is computed by scaling the sum $f_1 + f_2$ with the area weighting factor $\frac{|s|}{|s_h|}$, where $|s_h|$ is the area of the face $x_6x_4x_5x_8$. Similarly, if the cell face contacts with two boundary faces as in case (c), the flux is easily approximated by $f = f_1 \frac{|s|}{|s_q|}$, where $|s_q|$ is the area of the face $x_0x_7x_5x_8$.

3 Numerical convergence

The numerical examples in this section are designed by the benchmark session of the FVCA6 conference (June 2011, Praha [25]), where many interesting meshes are provided and 16 contributed numerical schemes are compared. However, the MPFA L-method is not included. Therefore, two 3D benchmark problems are taken here to study the numerical convergence of the L-method in comparison to TPFA and the MFD method. The TPFA method approximates the flux like explained for the MPFA boundary handling [equation (2.12)], the MFD method is implemented following [1] and [14]. For both examples, the problem (2.1) on $\Omega = (0, 1) \times (0, 1) \times (0, 1)$ is considered,

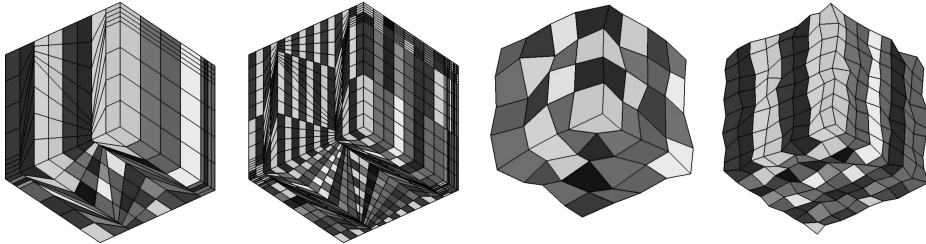


Figure 2.4: Kershaw meshes $8 \times 8 \times 8$ and $16 \times 16 \times 16$ (left), random meshes $4 \times 4 \times 4$ and $8 \times 8 \times 8$ (right).

and two kinds of meshes are tested. One is the 3D version of Kershaw's “z-mesh” [31] with planar faces. It is very challenging since some of its hexahedrons have faces that intersect at very acute angles which yield high skewness, see the left two graphs in Figure 2.4. The other one is a random mesh with nonplanar faces, see Figure 2.4 (right). Since irregular hexahedrons asymptotically become parallelepipeds and finally cuboides if a grid is uniformly refined, most numerical schemes would finally converge. Therefore, the Kershaw and the random mesh are refined on each level by preserving the same local geometrical structure.

Throughout the rest of this section, the convergence order graphs of the pressure and the normal velocity for various numerical simulations are shown and studied, where n_{dof} is the number of degrees of freedom. The relative discrete, mesh dependent L^2 norms of the error for the pressure e_p and the normal velocity e_v , are defined by

$$e_p = \left(\frac{\sum_{K \in \mathcal{T}_h} |K| (p_{\text{ex},K} - p_K)^2}{\sum_{K \in \mathcal{T}_h} |K| p_{\text{ex},K}^2} \right)^{\frac{1}{2}},$$

$$e_v = \left(\frac{\sum_{K \in \mathcal{T}_h} \sum_{j \in \partial K} |K| (\nu_{\text{ex},j}^\perp - \nu_j^\perp)^2}{\sum_{K \in \mathcal{T}_h} \sum_{j \in \partial K} |K| (\nu_{\text{ex},j}^\perp)^2} \right)^{\frac{1}{2}}.$$

Here, p_K is the discrete pressure solution of cell $K \in \mathcal{T}_h$. The analytical pressure value $p_{\text{ex},K}$ is evaluated at the cell center, $|K|$ is the cell area. The analytical normal velocity $\nu_{\text{ex},j}^\perp$ is evaluated by $-\mathbf{K} \nabla p \cdot \mathbf{n}$ at the face center, where \mathbf{n} is the unit outer normal of the cell face $j \in \partial K$. The discrete normal velocity ν_j^\perp is calculated at the face center. For $i \geq 2$, the convergence order $\text{cgl2}(i)$ of the L^2 norm of the error on the solution between grid level i and $i - 1$ can be obtained as

$$\text{cgl2}(i) = -3 \frac{\log(e_m(i)/e_m(i-1))}{\log(n_{\text{dof}}(i)/n_{\text{dof}}(i-1))}, \quad m = p \text{ or } v. \quad (2.13)$$

3.1 Benchmark test 1

Test 1 solves equation (2.1) with the permeability tensor

$$\mathbf{K} = \begin{pmatrix} 1 & 0.5 & 0 \\ 0.5 & 1 & 0.5 \\ 0 & 0.5 & 1 \end{pmatrix} \quad (2.14)$$

which is mildly anisotropic but defines three principal directions not aligned with the coordinate axes. Its exact solution is $p = 1 + \sin(\pi x) \sin(\pi(y + \frac{1}{2})) \times \sin(\pi(z + \frac{1}{3}))$.

3.1.1 Kershaw mesh

Test 1 is first run on the Kershaw mesh. Column (a) of Figure 2.5 shows the convergence behavior of the pressure and the normal velocity for the TPFA, the MPFA L-method using s_1 - and \tilde{s}_1 -criterion and the MFD method. It can be seen that the TPFA does not converge at all, and its quantitative errors do not reduce with the refinement.

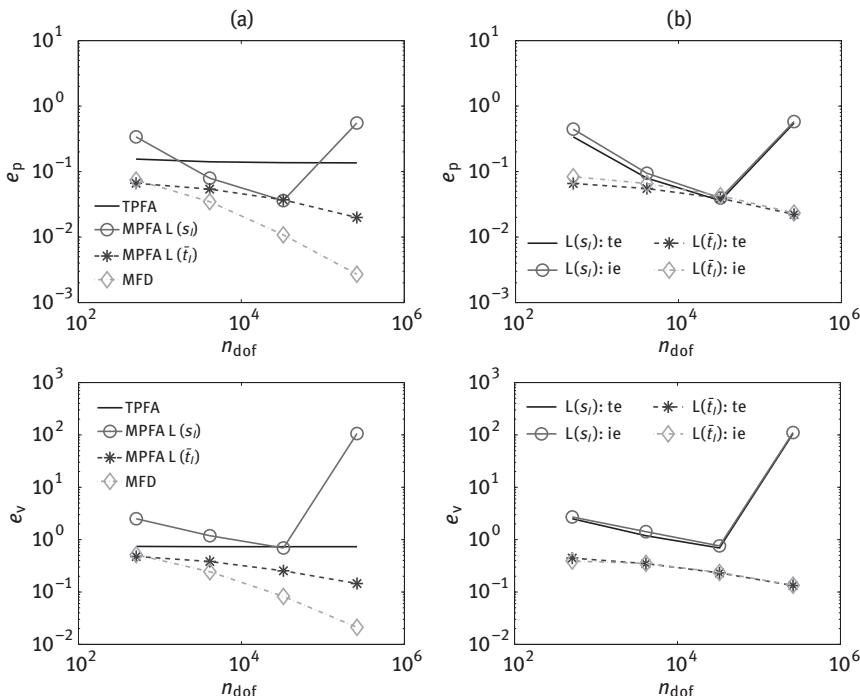


Figure 2.5: Numerical comparison of the pressure (upper row) and the normal velocity (lower row) for test 1 on the Kershaw mesh: (a) convergence behavior of different methods, (b) boundary effect on the convergence of the L-method using s_1 - and \tilde{s}_1 -criterion.

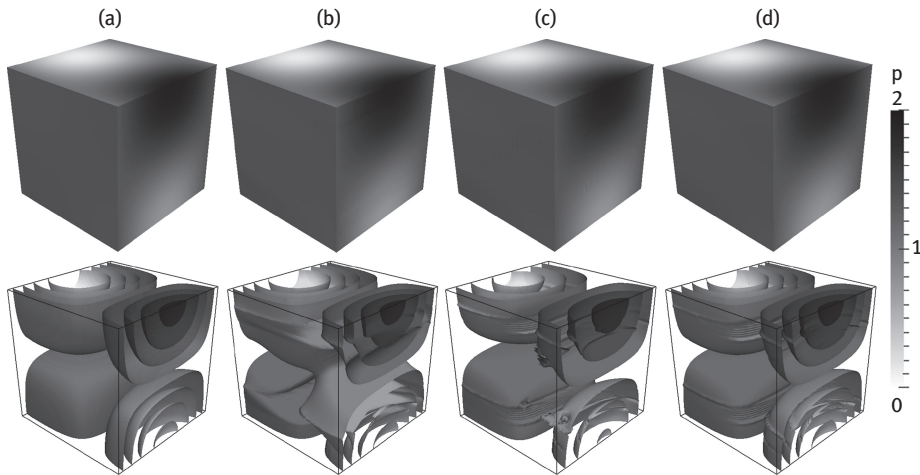


Figure 2.6: 3D surface graphs (upper row) and pressure isosurfaces (lower row) of different methods: (a) exact solution, (b) TPFA method, (c) MPFA L-method (s_l), (d) MFD method for test 1 on the Kershaw mesh $64 \times 64 \times 64$.

The 3D isosurface in the lower row of Figure 2.6 (b) clearly presents the distortion of the TPFA result which is affected by the anisotropy and the grid shape. In contrast, the MFD method converges very fast for both the pressure and the velocity with the order $\mathcal{O}(h^2)$, which can be indirectly seen from Figure 2.5(a) by calculating equation (2.13). The surface graph and the isosurfaces in Figure 2.6 (d) match well with the exact solution. However, the numerical solution of the L-method using the s_l -criterion blows up for the very fine mesh. Its convergence is mainly destroyed by extremely large errors in some local regions where the mesh has high skewness. Some of those regions can be identified in Figure 2.6 (c) or even better in the upper row of Figure 2.7 (b)–(d).

It is obvious that the s_l -criterion does not lead to proper L-stencils in some regions of this difficult example, and this motivates the development of the \bar{s}_l -criterion (2.11). Figure 2.5 (a) shows the convergence improvement of the \bar{s}_l -criterion for both the pressure and the velocity. The regions of oscillating pressure disappear from the pressure isosurfaces and from the slices of the L-solution shown in Figure 2.7 (b)–(d), lower row. To analyze differences between the two criteria the averaged size of the cell stencils is shown in Table 2.3 for different levels of the Kershaw mesh. The average is based on the flux stencils of all cells not lying on the boundary. It can be observed that the \bar{s}_l -criterion leads to slightly larger flux stencils. Additionally, the average stencil using the s_l -criterion decreases with increased refinement levels, which means that the flux stencils change for the finer grid. This change coincides with the change in the convergence behavior (Figure 2.5) and the appearance of the numerical instabilities. To investigate these effects in more detail, a simplified test for the L-selection

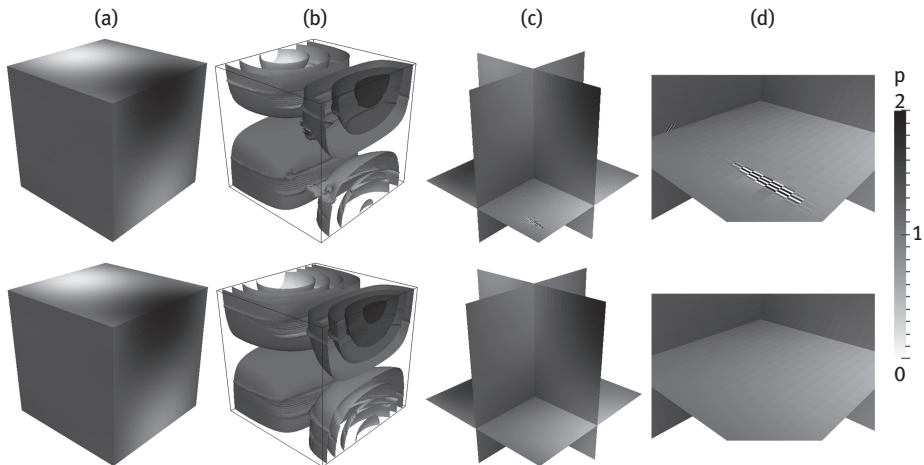


Figure 2.7: Comparison of the MPFA L-method using the s_l -criterion (upper row) and the \bar{t}_l -criterion (lower row) for test 1 on the Kershaw mesh $64 \times 64 \times 64$. (a) Surface pressure plots, (b) pressure isosurfaces, (c) viewing mode of three intersecting orthogonal slices, (d) zoom into the lower part of (c).

Table 2.3: Average size of the cell stencils resulting from the two L-selection criteria for benchmark test 1 on the Kershaw mesh.

Criterion \ Grid (cells)	Kershaw 8 (512)	Kershaw 16 (4096)	Kershaw 32 (32768)	Kershaw 64 (262144)
s_l	15	15	14	14
\bar{t}_l	18	18	18	18

criteria is shown and discussed at the end of this subsection. Although the performance of the L-method in this test case is improved by using the \bar{t}_l -criterion, the MFD method is still superior.

Concerning the simplified boundary discretization of the L-method, the total error (te) on the whole domain Ω and the inner error (ie) on the inner domain (Ω without the boundary layer of cells) are fairly close for both criteria, see Figure 2.5(b). This confirms the good performance of this boundary treatment. The first row of Figure 2.6 further tells us that this test case itself is not challenging for the boundary approximation since the pressure distribution on the boundary of the TPFA method matches well with the exact solution. Thus, we conclude that TPFA in combination with the area weighting approach often is sufficient.

Comparison of the L-selection criteria with regard to the grid skewness

To analyze the error resulting from the choice of the L-shape (Figures 2.5 and 2.7), a domain discretized by a $3 \times 3 \times 3$ parallelepiped mesh is considered. Again equation (2.1) is solved with the homogeneous anisotropic permeability tensor (2.14) which is visualized as ellipsoid in Figure 2.8.

Figure 2.9 shows the flux stencils of the center cell applying the two L-selection criteria for differently skewed grids. In case (a) with cubic cells the s_l -criterion chooses a flux stencil of minimal size that is perfectly aligned with the permeability tensor.

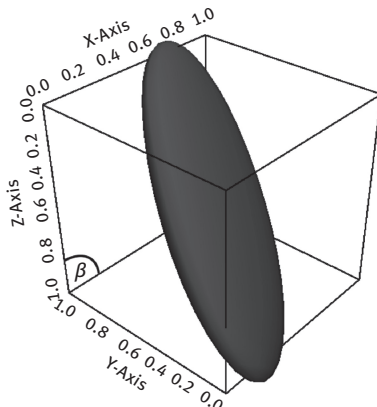


Figure 2.8: Visualization of the anisotropic permeability tensor (ellipsoid) inside the test domain.

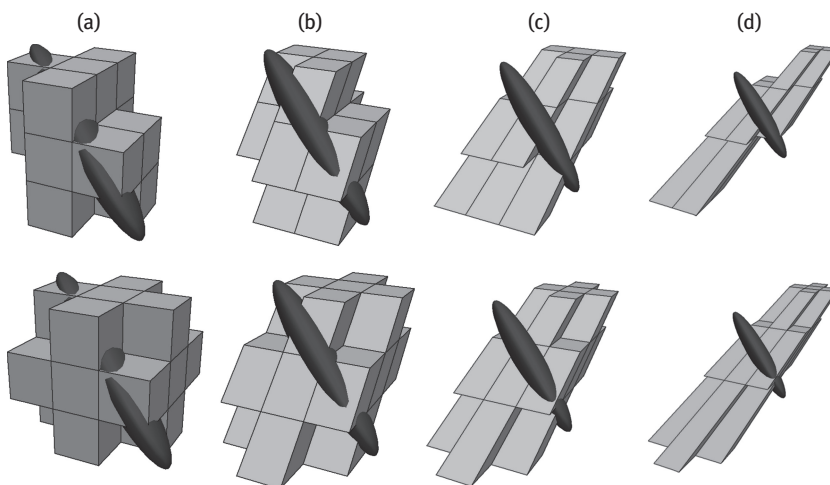


Figure 2.9: Cell stencils for differently skewed parallelepipeds grids using the s_l -criterion (upper row) and the \tilde{t}_l -criterion (lower row). The skewness of the grid is increased from left to right by decreasing the angle β (Figure 2.8): (a) 90° , (b) 45° , (c) 22.5° , (d) 11.25° .

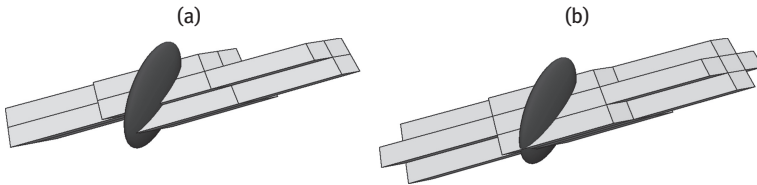


Figure 2.10: Top view on the cell stencils of the s_l -criterion (a) and the \bar{t}_l -criterion (b) for $\beta = 11.25^\circ$.

The \bar{t}_l -criterion chooses a larger stencil which is actually the maximal L-stencil. From Figure 2.9 (a) to (d) the angle β (Figure 2.8) is decreased. The stencil selected by the \bar{t}_l -criterion remains the same, whereas the stencil selected by the s_l -criterion changes. The preferred direction of the flux stencil, which results from the s_l -criterion, turns from case (a) to case (d) compared to the direction of the permeability tensor. This becomes even more obvious when looking down from the top (Figure 2.10). For this very skewed grid with $\beta = 11.25^\circ$, the preferred direction of the chosen flux stencil is opposite to the main direction of the permeability tensor. Therefore, the stencil most likely does not lead to a meaningful flux approximation. In contrast, the flux stencil using the \bar{t}_l -criterion better covers the main direction of the permeability tensor, and thus, well supports the skewed grids.

To summarize, the s_l -criterion tends to minimize the flux stencil while the \bar{t}_l -criterion results in larger stencils. Comparing the shape of the stencils, the s_l -criterion is more selective with regard to certain directions. In the grid cells with large skewness it appears that, the preferred direction of the flux stencil strongly differs from the direction of the streamlines. This also explains the large errors shown in Figure 2.6 (c). In such cases the cell stencil of the \bar{t}_l -criterion still leads to consistent fluxes. However, the robustness is increased at the cost of slightly larger stencils.

3.1.2 Random mesh

Next, we rerun test 1 on the random mesh to see the influence of the grid on the performance of different numerical methods. From Figure 2.11(a) we can see that the L-method using the s_l -criterion now can work properly with $\mathcal{O}(h^1)$ convergence order for the pressure and the normal velocity, while the convergence rate of the velocity for the MFD method is decreased compared to the Kershaw mesh. As expected, the TPFA cannot get the correct solution for any non-K-orthogonal grid whether with high or low skewness. For this test case, the two L-method selection criteria give similar results. This can also be seen from the lower row of Figure 2.12 where the solutions of the L-method and the MFD method are quite similar and close to the exact result. The inner pressure distribution of the TPFA does not catch the anisotropy correctly.

The most interesting aspect pointed out from the random mesh is that the non-planar surfaces have a bigger impact on the accuracy of the simplified boundary ap-

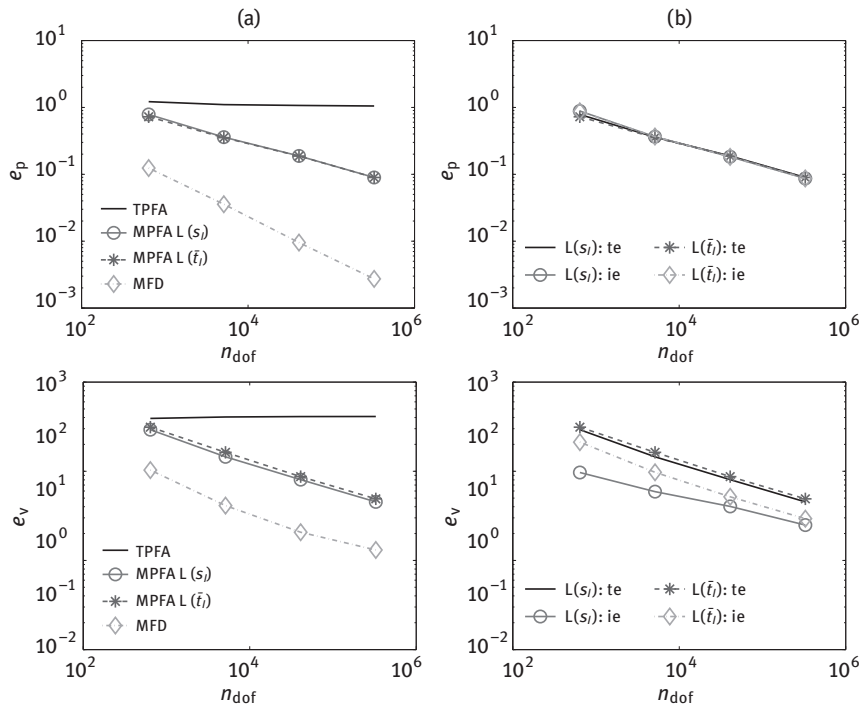


Figure 2.11: Numerical comparison of the pressure (upper row) and the normal velocity (lower row) for test 1 on the random mesh: (a) convergence behavior of different methods, (b) boundary effect on the convergence of the L-method using s_I - and \tilde{t}_I -criterion.

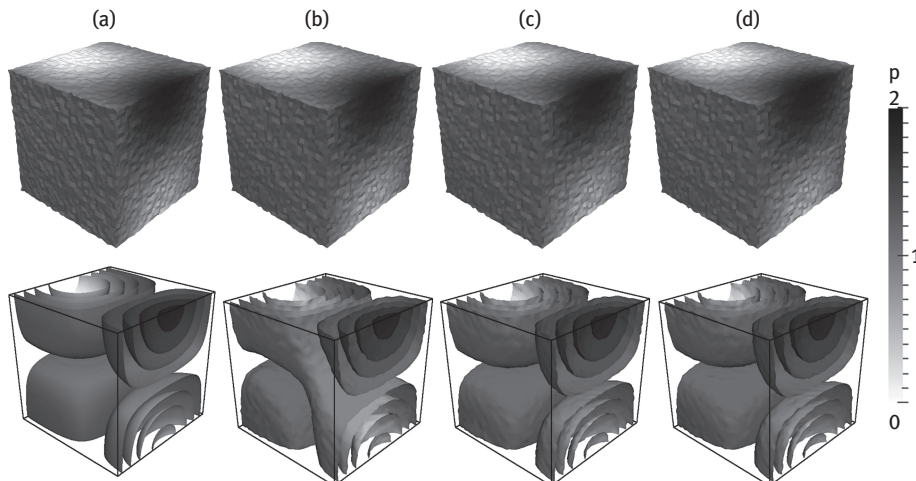


Figure 2.12: 3D surface graphs (upper row) and pressure isosurfaces (lower row) of different methods: (a) exact solution, (b) TPFA method, (c) MPFA L-method (s_I), (d) MFD method for test 1 on the random mesh $32 \times 32 \times 32$.

proximation of the L-method. For both selection criteria, the quantitative error of the normal velocity is increased whereas the pressure is less sensitive to the boundary handling, see Figure 2.11 (b). In comparison, the L-method using the \bar{t}_I -criterion yields a smaller boundary error for the normal velocity than the method using the s_I -criterion.

3.2 Benchmark test 3

Test 3 solves equation (2.1) with the exact solution $p = \sin(2\pi x) \sin(2\pi y) \sin(2\pi z)$ and the permeability tensor

$$\mathbf{K} = \begin{pmatrix} 1 & 0 & 0 \\ 0 & 1 & 0 \\ 0 & 0 & 10^3 \end{pmatrix}. \quad (2.15)$$

Obviously, the tensor has a relatively high anisotropy ratio, and its principal directions coincide with the coordinate axes. So the Kershaw mesh is very non-K-orthogonal in the inner local regions, whereas the random mesh is quite close to a K-orthogonal grid.

3.2.1 Kershaw mesh

Compared to test 1 on the Kershaw mesh, for test 3 the L-method quantitatively gets better solutions than the MFD method for both the pressure and the normal velocity, see Figure 2.13 (a). Since the Kershaw mesh is non-K-orthogonal in terms of the tensor (2.15), the TPFA still fails to converge and its pressure solution exhibits undershoot/overshoot with the magnitude $[-3.32, 3.32]$ as seen from Figure 2.14 (b). Compared to the full permeability tensor in test 1, the simulation of test 3 on the Kershaw mesh is not so challenging. Thus, the s_I -criterion as well as the \bar{t}_I -criterion lead to almost the same numerical results, see Figure 2.13 (a). Again, the simplified L-boundary implementation is sufficiently accurate for both criteria.

3.2.2 Random mesh

Compared to the three other simulation cases, the random mesh with the diagonal tensor (2.15) is slightly better suited for the TPFA method. One obtains $\mathcal{O}(h^1)$ convergence for the pressure, but the relatively big error is amplified for the normal velocity resulting in a loss of convergence, see Figure 2.15 (a). The L-method using the \bar{t}_I -criterion generates a larger error for the normal velocity than the s_I -criterion; however the difference is not significant. Both the L-methods are still quantitatively better than the MFD method. Since the boundary faces of the random mesh are nonplanar, the boundary errors in Figure 2.15 (b) are bigger than those for test 3 on the Kershaw

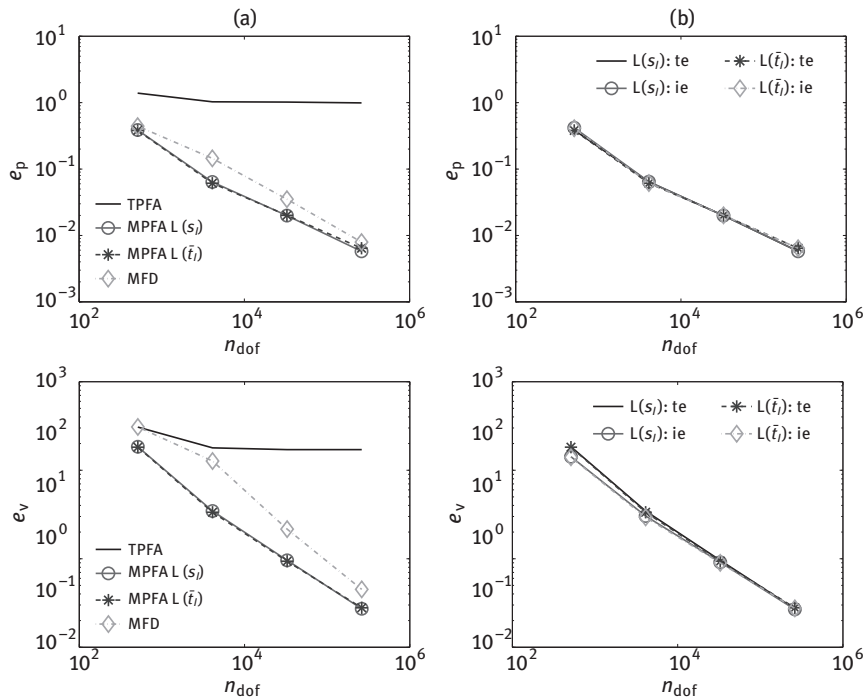


Figure 2.13: Numerical comparison of the pressure (upper row) and the normal velocity (lower row) for test 3 on the Kershaw mesh: (a) convergence behavior of different methods, (b) boundary effect on the convergence of the L-method using s_I - and \bar{t}_I -criterion.

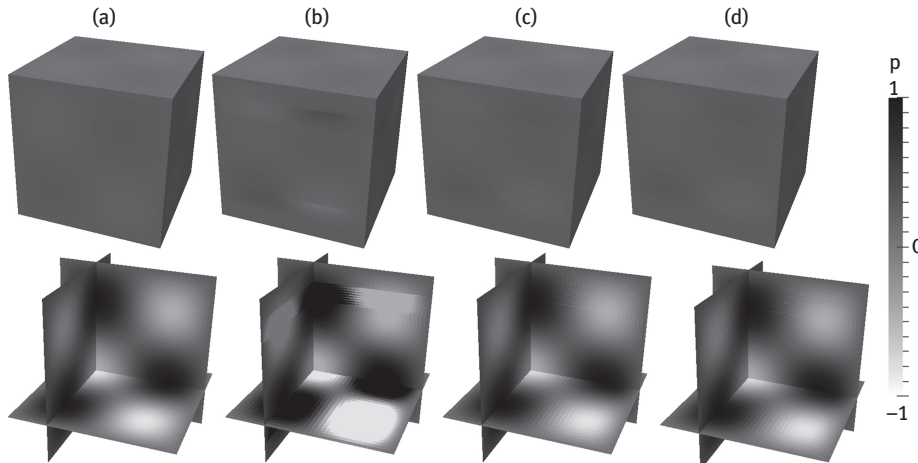


Figure 2.14: 3D surface graphs (upper row) and the viewing mode of three intersecting orthogonal slices (lower row) of different methods: (a) exact solution, (b) TPFA method, (c) MPFA L-method (s_I), (d) MFD method for test 3 on the Kershaw mesh $64 \times 64 \times 64$.

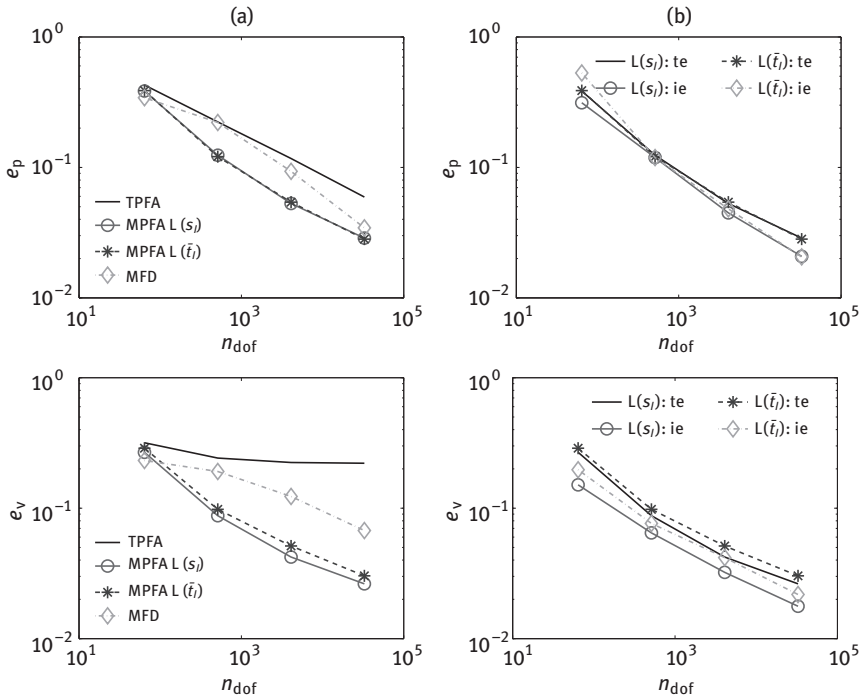


Figure 2.15: Numerical comparison of the pressure (upper row) and the normal velocity (lower row) for test 3 on the random mesh: (a) convergence behavior of different methods, (b) boundary effect on the convergence of the L-method using s_1 - and \tilde{t}_I -criterion.

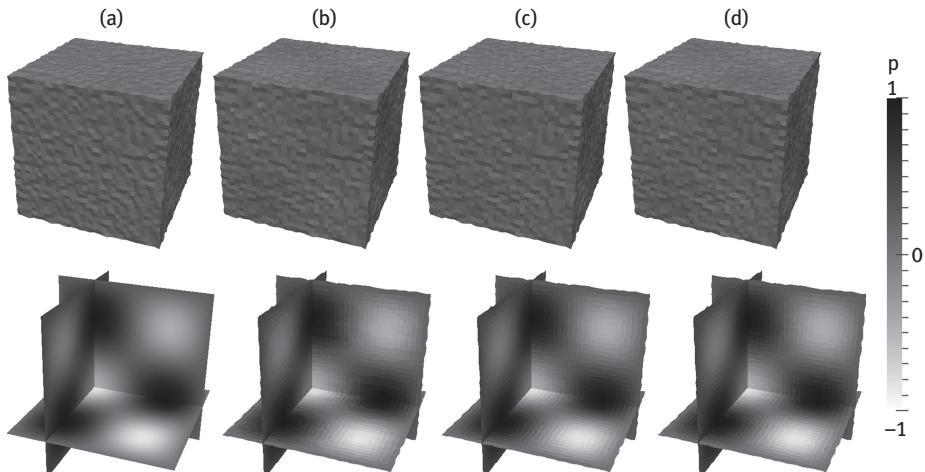


Figure 2.16: 3D surface graphs (upper row) and the viewing mode of three intersecting orthogonal slices (lower row) of different methods: (a) exact solution, (b) TPFA method, (c) MPFA L(s_1), and (d) MFD method for test 3 on the random mesh $32 \times 32 \times 32$.

mesh. Although the TPFA solution in Figure 2.16 is more accurate than in the former cases, we still see some inner grid cells with small artificial oscillations.

As a conclusion, the robustness of the L-method is determined by the criterion for choosing the proper L-stencil. The \bar{t}_1 -criterion can handle all test cases, and it seems to be more robust than the s_1 -criterion. The boundary discretization proposed in Section 2.3 is demonstrated to be efficient and accurate enough. Most importantly, it is trivial to implement, can be easily applied to more complex domain shapes, and can be used in the case of adaptive mesh refinement (see Section 4). These examples show the superiority of the L-method over the TPFA, and moreover both the L-method and the MFD approach provide qualitatively similar results. While the MFD method is superior for the first test case with mild anisotropy and a full permeability tensor, the L-method yields better results for the second test case with strong anisotropy and a diagonal permeability tensor.

Besides robustness and accuracy, efficiency of a method is crucial. In Table 2.4, assembler and linear solver times for the different methods are exemplarily shown for test 1 on Kershaw grid $32 \times 32 \times 32$. The TPFA method is much faster than both other methods. While the computing time for assembling the linear system is in the same order of magnitude for TPFA and MFD method, the MPFA method is much more expensive. The reason is the complex construction of the transmissibility matrices explained before. However, the linear solver time of the MPFA method is only slightly larger than of the TPFA method while the solution of the MFD system is much more expensive. Thus, in total the solution time of MPFA and MFD method is very similar. As the assembling time scales approximately linear with system size, while the linear solver time does usually not, the linear solver becomes more and more dominating with regard to efficiency if the grid size is increased. In this case the larger number of degrees of freedom of the MFD method, compared to TPFA and MPFA method, can stronger affect efficiency as the complex assembling of the linear system of the MPFA method. We point out that the L-method always gives rise to a purely pressure based system with one degree of freedom per element. This is not the case for the MFD and other mixed schemes. Usually, the assembly of flux and pressure degrees of freedom associated with faces and elements results in a linear system that exhibits sad-

Table 2.4: Averaged assembler and linear solver times from 10 model runs for benchmark test 1 on Kershaw grid $32 \times 32 \times 32$ (32768 cells), using the same linear solver on the same hardware.

	TPFA	MPFA	MFD
Assembler time (s)	0.18	3.96	0.55
Solver time (s)	5.55	6.99	11.08
Assembler time + Solver time (s)	5.73	10.95	11.63
$\frac{\text{Assembler time}}{\text{Solver time}}$	0.03	0.57	0.05

dle point structure and, therefore, is approximately four times larger (for hexahedral meshes) and harder to solve. The classical remedy for this problem of the mixed approaches is hybridization by means of introducing face pressure degrees of freedom and allowing to locally eliminate the original unknowns. While this yields a symmetric positive definite system of linear equations, the number of degrees of freedom still is three times as large as for a purely cell-centered method. In [47], a strategy is provided for the local elimination of the flux unknowns for the lowest-order mixed method yielding a system with only element degrees of freedom. While this approach is attractive for simplicial meshes, its application to hexahedral grids would involve larger patches of elements for the solution of local problems and therefore larger stencils than for the L-method.

4 Grid adaptivity

Regarding time-dependent coupled transport problems like multiphase flow in porous media, the efficiency of the numerical method is crucial. Complex discretization schemes like the MPFA L-method might not be applicable for large-scale problems on very fine meshes. One way to increase efficiency is to use locally refined grids. We adapt the grid by nonconforming grid refinement allowing one hanging node per cell face. The macro grid is assumed to be conforming. An advantage of the L-method is that the treatment of hanging nodes is straightforward.

Figure 2.17 shows the basic types of interaction volumes which can occur around a hanging node. The flux faces corresponding to these interaction-volume shapes are sketched in Figure 2.18. For each flux face of an interaction volume around a hanging-node the flux can be calculated by applying one of the four L-stencils introduced in Figure 2.2. However, compared to a regular node only one or one of two of these L-shapes can be suitable for certain flux faces. For instance, for the volume Type 1, all four L-cases could be used for the flux calculation through faces 1–4, while only the stencil (a) or (b) could be used for the flux faces 9–12, see Figure 2.18. Let us consider the L-stencil for face 9 of the volume Type 1, where the cell number 5 is cell 1 according to the numbering of Figure 2.2 and the cell number 1 is cell 2. In this case, only cells 5, 1, 3, and 2 can be combined to the regular L-shape (b). The remaining three L-shapes, respectively, combine cells 5 and 1 for the construction of the L-stencil (a), cells 5, 1, and 3 for the L-stencil (c), and cells 5, 1, and 2 for the L-stencil (d), which lead to stencils consisting of less than four cells. Obviously, these degenerated stencils are not feasible to derive a closed local system for the flux approximation through face 9.

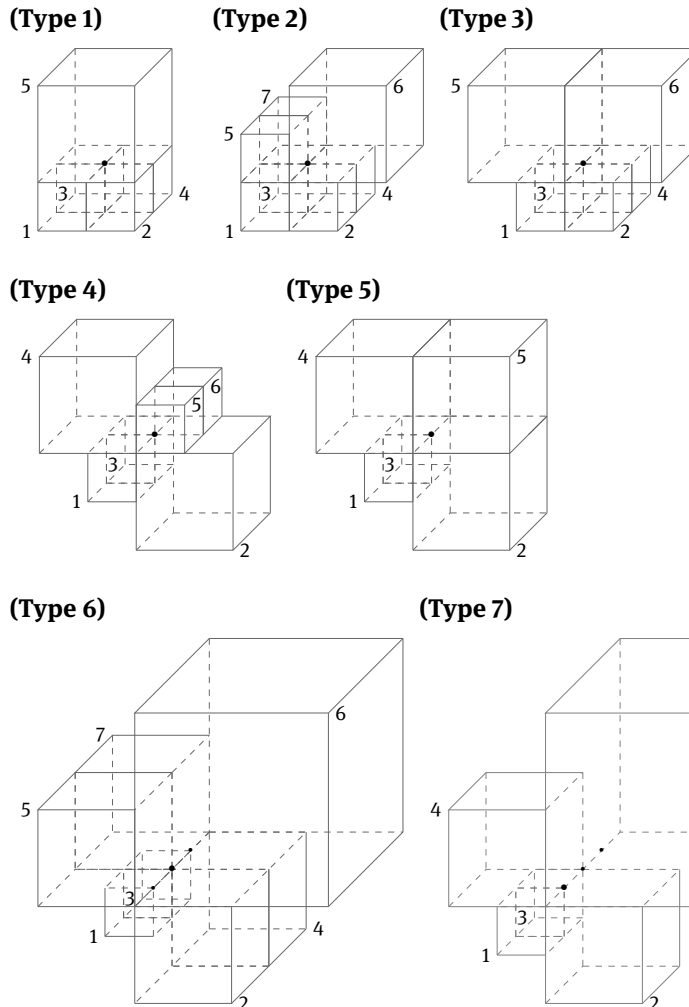


Figure 2.17: Interaction-volume-types around hanging nodes allowing only one hanging node (HN) per cell face. (Type 1): one face HN; (Type 2): one edge HN, one coarser cell; (Type 3): one edge HN, two coarser cells; (Type 4): one edge HN, two coarser cells, diagonal configuration; (Type 5): one edge HN, three coarser cells; (Type 6): three edge HNs, special case of (Type 2); (Type 7): three edge HNs, special case of (Type 5).

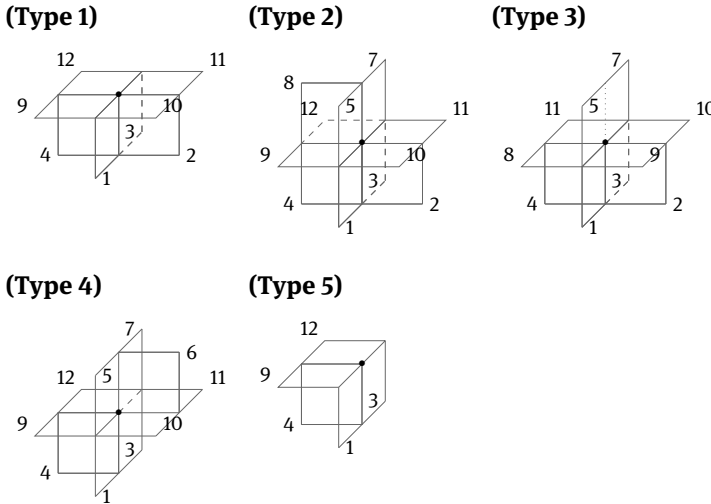


Figure 2.18: Flux faces of the different interaction-volume-types shown in Figure 2.17. The numbering of the faces relates to the general case without hanging nodes (12 faces per interaction-volume). (Type 1): 8 flux faces; (Type 2): 11 flux faces; (Type 3): 10 flux faces; (Type 4): 10 flux faces; (Type 5): 5 flux faces; (Type 6): see (Type 2); (Type 7): see (Type 5).

4.1 Boundary handling

As explained in Section 2.3, the TPFA is used at Dirichlet boundaries and a weighting factor is used to obtain the fluxes through the faces intersecting with the boundary. If hanging nodes occur, the weighting becomes more complex. Considering two neighboring cells of the interaction volume around a hanging node, the intersecting face of one (coarser) cell could touch a boundary while the intersecting face of the other (finer) cell could be completely inside the domain. Figure 2.19 exemplarily shows such a situation. The hatched area marks a boundary face. The shaded area is the area through which the flux is calculated by the MPFA interaction volumes inside the model domain (volumes that do not touch the boundary). Each of the arrows in Figure 2.19 (a) represents the flux f_i through a subinterface i of the interface $x_5x_6x_3x_4$ calculated from one L-stencil. Similarly for the nonadaptive case explained before we now want to weight the flux through the interface $x_5x_6x_3x_4$ such that it approximates the flux through the interface $x_1x_2x_3x_4$. According to Section 2.3, we can define

$$f = \frac{|s|}{\sum_i |s_i|} \sum_i f_i, \quad (2.16)$$

where $|s_i|$ is the area of the flux subinterface i and $|s|$ the reference face area. However, instead of two cells sharing one face we now have five cells. Thus, we have

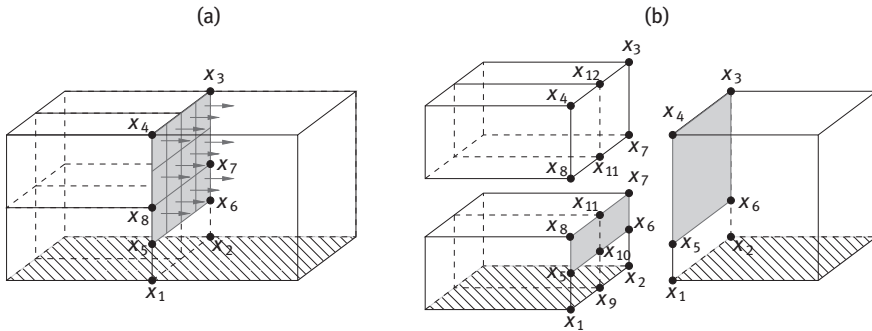


Figure 2.19: Example for boundary treatment with hanging nodes. The hatched area marks the boundary faces. (a) MPFA flux area (shaded) and subfluxes (arrows) – Fluxes are not calculated by the MPFA for the whole cell face! (b) MPFA flux area (shaded) only for the boundary cells.

to weight separately for each of the five cells (Figure 2.19 (b)). The two upper left cells intersecting at subfaces $x_8x_{11}x_{12}x_4$ and $x_{11}x_7x_3x_{12}$ are not located directly at the boundary. For these cells, we have $|s|/\sum_i |s_i| = 1.0$. For the remaining cells, the flux is approximated by equation (2.16) with

- one right coarse cell: $i = i \in x_5x_6x_3x_4$ and $|s| = \text{area of face } x_1x_2x_3x_4$;
- two lower left fine cells:
 - $i = i \in x_5x_{10}x_{11}x_8$ and $|s| = \text{area of face } x_1x_9x_{11}x_8$, and
 - $i = i \in x_{10}x_6x_7x_{11}$ and $|s| = \text{area of face } x_9x_2x_7x_{11}$.

Equation (2.16) is general and can be applied to any kind of boundary configuration, with f_i being the subflux through one subinterface calculated from nonboundary MPFA interaction volumes, $|s|$ the cell face area and $|s_i|$ the area of subinterface i . If a face does not intersect with a boundary, $|s| = \sum_i |s_i|$ and $f = \sum_i f_i$.

5 Two-phase flow applications

In this section the 3D MPFA L-method is applied to two-phase flow in porous media. Various discretization schemes, like the MFD method used for the comparison in Section 3, are able to handle elliptic equations with complex coefficients on complex grids. However, in case of two-phase flow additionally the correct and conservative transport of phases, described by a parabolic transport equation, is important. Therefore, physical features like saturation discontinuities at fluid fronts or at heterogeneous material interfaces have to be reproduced by the numerical scheme. For regular K-orthogonal grids, the finite volume method with TPFA is a very powerful scheme, which is naturally very well suited to account for effects like saturation discontinuities at material interfaces (capillary pressure interface conditions [28]). For non-K-orthogonal meshes or at interfaces with hanging nodes, for example from local

grid adaption, the correct flux approximation is difficult or not possible. Alternative methods like MFD are very flexible with regard to grids and anisotropic coefficients. In the simplified case, in which we neglect capillary-pressure effects, the two-phase pressure equation (2.24) can be formulated in a similar form as the previously discussed one-phase equation (2.1). Thus, the application of MFD and other mixed methods is straightforward. However, in the complex case with capillary pressure, an additional term appears in the pressure equation. Correct treatment of capillary effects, especially in the case of heterogeneous capillary-pressure functions, is challenging. The flux approximation depends on the capillary-pressure values at the cell faces. To approximate these values at the heterogeneous material interfaces, additional equations, conditions and thus also degrees of freedoms could be added to the system of equations or solved separately as an additional system of equations. The latter is for example proposed in [30] for a MFE method. To the authors' knowledge, no MFD method has been published that solves two-phase problems on heterogeneous domains with capillary pressure and gravity. For the proposed MPFA method, no additional equations or degrees of freedom are needed. In the following test cases, we compare the MPFA L-method to the TPFA. The intention is to investigate the capabilities of the L-scheme by verifying the MPFA L-model and showing the superiority of the MPFA over the TPFA. The test cases are an advection-dominated problem (Buckley–Leverett-type problem [15]), a capillary-diffusion-dominated problem (McWhorter-type problem [35]), and two denser-non-aqueous-phase-liquid (DNAPL) infiltration scenarios. The tests include homogeneous as well as heterogeneous, and isotropic as well as anisotropic porous media, without or with capillary pressure on structured and unstructured grids.

5.1 Two-phase model description

Assuming immiscible incompressible fluids under isothermal conditions, the two-phase flow system can be described by the saturation conservation equations of each fluid phase:

$$\phi \frac{\partial S_w}{\partial t} + \nabla \cdot \mathbf{v}_w = q_w, \quad (2.17)$$

$$\phi \frac{\partial S_n}{\partial t} + \nabla \cdot \mathbf{v}_n = q_n. \quad (2.18)$$

The two fluid phases are indicated by the subscripts w (wetting) and n (nonwetting), S is the saturation, ϕ is the porosity of the porous medium, and q a source term. With the constitutive relation $S_w + S_n = 1$, equations (2.17) and (2.18) can be combined to one pressure equation

$$\nabla \cdot \mathbf{v}_t = q_t, \quad (2.19)$$

where $\mathbf{v}_t = \mathbf{v}_w + \mathbf{v}_n$ is the total velocity. To solve the system of the pressure equation (2.19) and the saturation transport equation (2.17), additional constitutive relations are needed:

$$\mathbf{v}_\alpha = -\frac{k_{r\alpha}}{\mu_\alpha} \mathbf{K} \nabla \Phi_\alpha, \quad \alpha = w, n, \quad (2.20)$$

$$p_c = p_n - p_w. \quad (2.21)$$

Equation (2.20) is Darcy's law for multiphase flow (e.g., [27, 42]), which relates the fluid phase velocity \mathbf{v}_α to the phase potential Φ_α . Further parameters are the absolute permeability of the porous medium \mathbf{K} , the relative permeability of a phase $k_{r\alpha}$, and the dynamic fluid viscosity μ_α . Equation (2.21) relates the phase pressures p_α to each other by the capillary pressure p_c . The capillary pressure as well as the relative phase permeabilities are commonly assumed to be functions of the saturation ($p_c := p_c(S_w)$, $k_{r\alpha} := k_{r\alpha}(S_\alpha)$). The phase potentials are defined as

$$\begin{aligned} \Phi_w &= p_w + \varrho_w g z, \\ \Phi_n &= p_n + \varrho_n g z \end{aligned} \quad (2.22)$$

with g being the gravity constant and z the distance to the reference plane orthogonal to the direction of gravity. Inserting equations (2.20)–(2.22) into equation (2.19) yields

$$\nabla \cdot [-\lambda_t \mathbf{K} (\nabla p_w + f_n \nabla p_c) - (\lambda_w \varrho_w + \lambda_n \varrho_n) g \nabla z] = q_t, \quad (2.23)$$

where $\lambda_\alpha = k_{r\alpha}/\mu_\alpha$ are phase mobilities, $\lambda_t = \lambda_w + \lambda_n$ is the total mobility, and $f_\alpha = \lambda_\alpha/\lambda_t$ are the phase fractional flow functions. Alternatively, the equation can be formulated for potentials [30, 49]

$$\nabla \cdot [-\lambda_t \mathbf{K} \nabla \Phi_w - f_n \lambda_t \mathbf{K} \nabla \Phi_c] = q_t, \quad (2.24)$$

where the capillary potential is defined as

$$\Phi_c = \Phi_n - \Phi_w = p_c + (\varrho_n - \varrho_w) g z. \quad (2.25)$$

As the primary unknown of the pressure equation is a phase pressure or potential the phase velocity can be directly calculated and thus equation (2.17) be directly solved as saturation transport equation.

The 3D MPFA L-model for two-phase flow used for the following examples is based on the potential formulation (2.24). Advantages of the potential formulation in general and combined with a MPFA method are discussed in Wolff et al. [49]. Pressure and saturation equations are solved sequentially applying an IMPES (IMplicit Pressure Explicit Saturation, e.g. [12]) algorithm. Phase mobilities for flux calculation are determined using an upstream weighting scheme. To guaranty stability of the IMPES scheme the criterion of [19] is applied.

5.2 Buckley–Leverett-type problem

The setup of this example is shown in Figure 2.20. The domain with the size of $30 \times 6 \times 3$ m has a constant porosity, a constant permeability ($\phi = 0.2$; $K = kI$, where $k = 10^{-7} \text{ m}^2$, I is the identity matrix) and is initially saturated by a nonwetting fluid. From one side a wetting fluid is injected and displaces the nonwetting fluid. Both fluids have the same fluid properties. Relative permeabilities are calculated using Brooks–Corey parameterizations with $\lambda = 2.0$ and residual saturations $S_{\text{wr}} = S_{\text{nr}} = 0.2$. Gravity as well as capillary effects are neglected. The reference solution of this problem calculated on a very fine structured grid is shown in Figure 2.21(b). To test the capabilities of the MPFA L-method, an unstructured grid used. The macro grid (level 0) consists of 32 cells. The level 1 grid (256 cells) is shown in Figure 2.21(a). Figure 2.22 shows a comparison of the results of the TPFA method and the L-method. From top to bottom the grid shown in Figure 2.21(a) is hierarchically refined from level 1 to level 4. It is obvious that the L-method converges to the reference solution with a limited number of grid refinements. In comparison, the TPFA method is not able to calculate correct fluxes for the unstructured grid and exhibits a curved shock front (Figure 2.23).

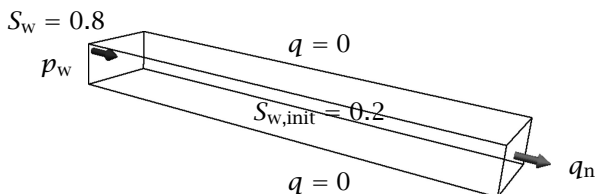


Figure 2.20: Setup of the Buckley–Leverett problem. The arrows mark the wetting fluid inflow and the nonwetting fluid outflow.

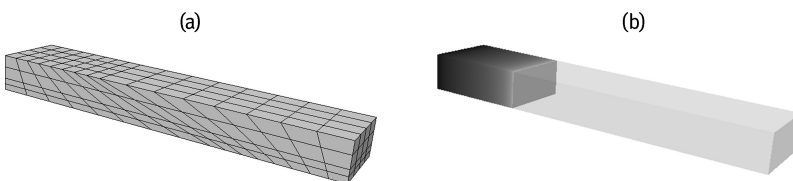


Figure 2.21: Simulation grid of level 1 (a) and the reference solution (b) of the Buckley–Leverett problem.

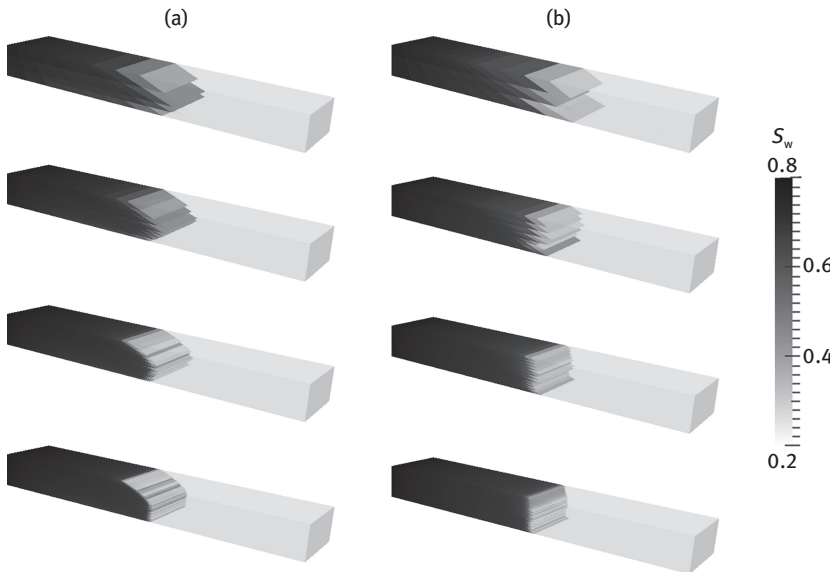


Figure 2.22: Water saturation of the Buckley–Leverett problem using (a) the TPFA method and (b) the MPFA L-method. From top to bottom the grid is refined from level 1 to level 4.



Figure 2.23: 2D slices in the x - z -plane, showing the water saturation of the Buckley–Leverett problem on the finest grid: (a) the reference solution, (b) the TPFA solution, (c) the MPFA L-solution.

5.3 McWhorter-type problem

The McWhorter problem is a capillary-diffusion-dominated flow problem. The model domain, again with the size of $30 \times 6 \times 3$ m, is initially fully saturated by a nonwetting fluid (Figure 2.24). All boundaries except one are no flow boundaries. The open boundary is a contact area between the nonwetting fluid inside the domain and a wetting fluid outside the domain. Due to the capillary-pressure gradient, counter-current flow develops. Porosity as well as permeability are constant ($\phi = 0.3$; $\mathbf{K} = k\mathbf{I}$, where $k = 10^{-10}$ m 2). Again both fluids have the same fluid properties and relative permeabilities are parameterized by Brooks–Corey functions ($\lambda = 2.0$, $S_{wr} = S_{nr} = 0$). Gravity is neglected. The reference solution is shown in Figure 2.25(b). Like for the Buckley–Leverett problem an unstructured grid is used (Figure 2.25(a)) and the L-method is compared to the TPFA method.

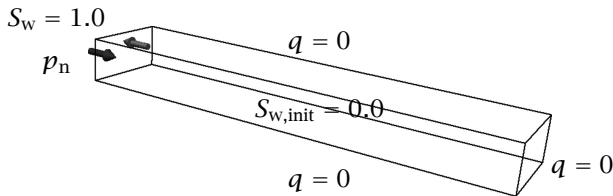


Figure 2.24: Setup of the McWhorter problem. The arrows mark the wetting fluid inflow and the nonwetting fluid outflow.

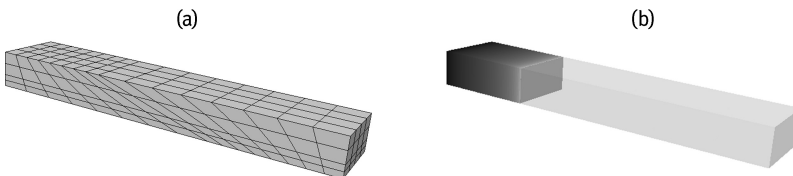


Figure 2.25: Simulation grid of level 1 (a) and the reference solution (b) of the McWhorter problem.

Also for the capillary-diffusion-dominated case the MPFA L-method converges to the reference solution when the grid is refined (Figure 2.26 (b)), while the front of the TPFA method is tilted following the direction of the skewed unstructured grid cells (Figure 2.27).

5.4 DNAPL infiltration problem

Finally, we test the grid adaptive MPFA L-method on two DNAPL infiltration scenarios. In case 1 the porous medium is assumed to be heterogeneous but isotropic, in case 2 it is assumed to be homogeneous but anisotropic.

The model domain of case 1 is shown in Figure 2.28. It is initially saturated with water. DNAPL infiltrates from the top of the domain at the location marked by the arrow. The bottom and top (except the infiltration area) are impermeable. On the side boundaries we apply hydrostatic pressure conditions and allow free fluid outflow (or inflow). Three low permeable lenses are marked by the anthracite boxes. The background permeability and entry pressure are $K_b = k_b I$ with $k_b = 10^{-10} \text{ m}^2$, $p_{d,b} = 500 \text{ Pa}$. Permeabilities and entry pressures of the lenses are $K_l = k_l I$ with $k_l = 10^{-14} \text{ m}^2$, $p_{d,l} = 5000 \text{ Pa}$. Relative permeabilities and capillary pressure are parameterized by Brooks–Corey functions. Porosity as well as the Brooks–Corey parameter λ are constant through the whole domain ($\lambda = 2.0$, $\phi = 0.4$). The domain size is chosen to be $20 \times 20 \times 10 \text{ m}$. We generate a structured coarse grid of $10 \times 10 \times 10$ cells, which just resolves the lenses. For the TPFA model this grid is globally

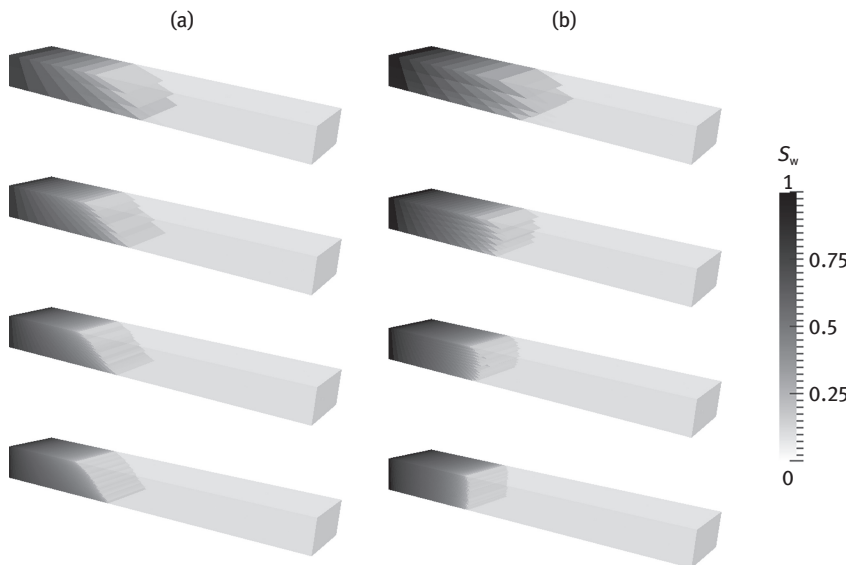


Figure 2.26: Water saturation of the McWhorter problem using (a) the TPFA method and (b) the MPFA L-method. From top to bottom the grid is refined from level 1 to level 4.

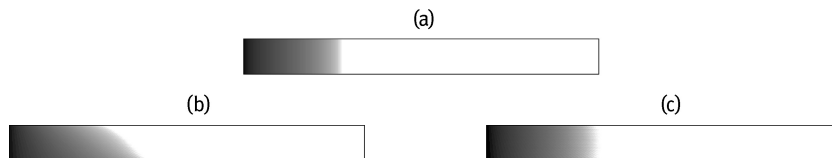


Figure 2.27: 2D slices in the x - z -plane, showing the water saturation of the McWhorter problem on the finest grid: (a) the reference solution, (b) the TPFA solution, (c) the MPFA L-solution.

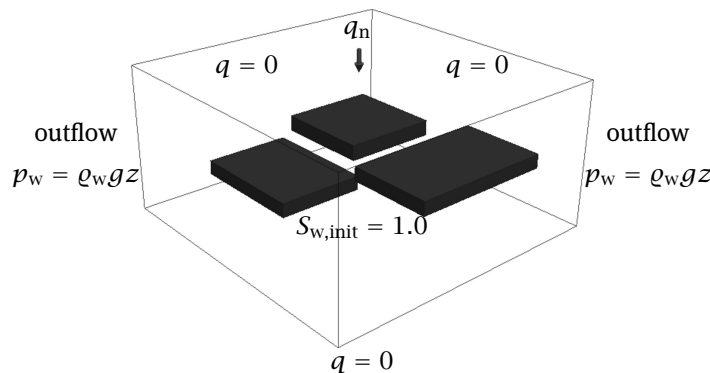


Figure 2.28: Problem setup of the DNAPL infiltration example. The arrow indicates where the DNAPL is released. The gray boxes are lenses of lower permeability and higher entry pressure.

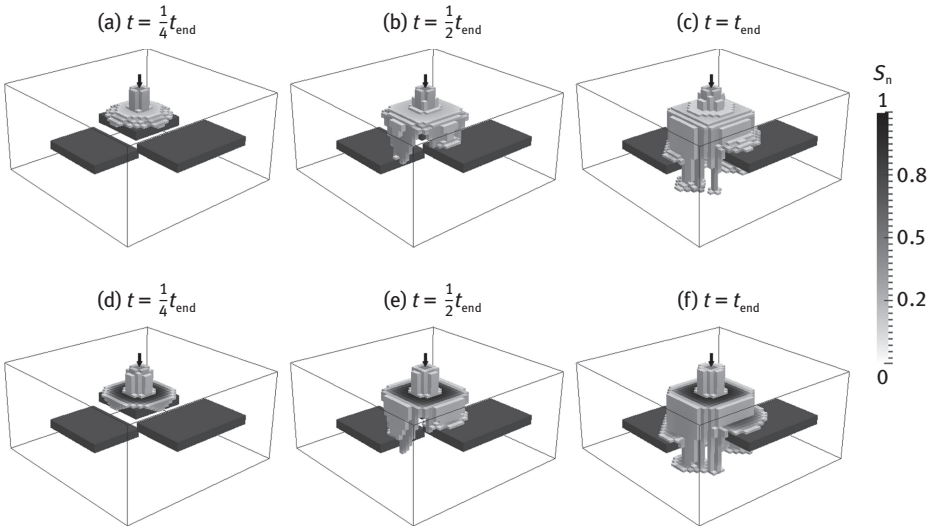


Figure 2.29: DNAPL infiltration case 1: (a)–(c) show the results of the TPFA method, (d)–(f) show the results of the adaptive MPFA L-method.

refined twice leading to a grid of $40 \times 40 \times 40$ cells. The adaptive MPFA L-model uses the coarse grid, but is allowed to locally refine the grid twice.

The results of DNAPL case 1 are plotted in Figure 2.29. Figure 2.29 (a)–(c) shows the results of the TPFA method and Figure 2.29 (d)–(f) of the adaptive MPFA L-method. Both methods show similar DNAPL saturation distributions. They account for the heterogeneities and also satisfy the interface condition due to the capillary-pressure heterogeneity (see e.g., [28]). However, the TPFA is more diffusive than the L-method. Considering the pooling on top of the lenses, the DNAPL layer from the L-model mainly consists of one cell layer while the DNAPL layer from the TPFA model consists of two or more cell layers. A possible reason is that due to the larger flux stencil the ability of the L-method to deflect the flow at the lens is higher. The same effect can be observed where the DNAPL flows round the corners of the lenses. The adaptive local grid refinement of the L-model is visualized in Figure 2.30. As can be observed from Figure 2.30 (a), mostly the coarsest grid cells are used at the early time of the simulation. Later, more and more cells are refined following the DNAPL distribution.

The setup of case 2 is similar to case 1 (Figure 2.28). DNAPL still infiltrates from the top at the location marked by the arrow. Boundary conditions remain the same. However, instead of the heterogeneities we now introduce anisotropy. The homogeneous anisotropic permeability tensor is defined as

$$\mathbf{K} = \begin{pmatrix} 10^{-10} & 0 & -5 \times 10^{-11} \\ 0 & 10^{-10} & 5 \times 10^{-11} \\ -5 \times 10^{-11} & 5 \times 10^{-11} & 5 \times 10^{-11} \end{pmatrix} \text{m}^2.$$

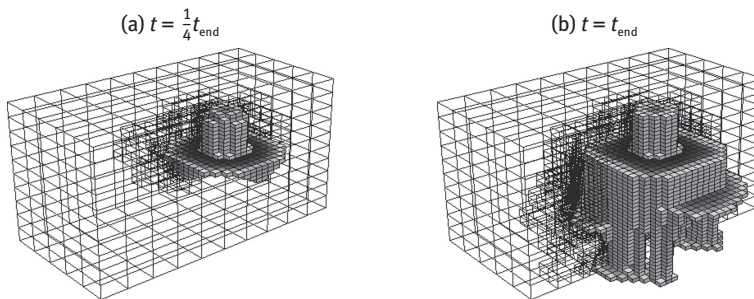


Figure 2.30: Locally adapted grids of the adaptive MPFA model for DNAPL case 1.

Further, a constant entry pressure $p_d = 5000$ Pa is used in the entire domain. For this case where no lenses have to be resolved by the grid, a structured coarse grid of $2 \times 2 \times 2$ cells is generated. This is globally refined to a $32 \times 32 \times 32$ grid for the TPFA model. The adaptive MPFA L-model again uses the coarse grid but is allowed to refine four times. Figure 2.31 shows the results of DNAPL case 2, where (a) and (b) are results of the TPFA model and (c) and (d) of the adaptive L-model. The TPFA clearly fails to account for the anisotropy in the off-diagonal direction. The DNAPL just follows the direction of gravity, which is the driving force, and pools at the impermeable bot-

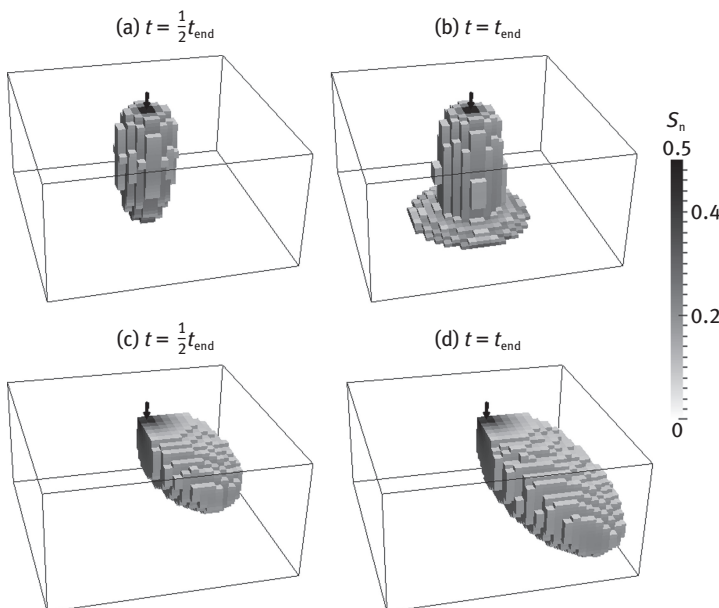


Figure 2.31: DNAPL infiltration case 2: (a) and (b) show the results of the TPFA method and (c) and (d) of the adaptive MPFA L-method.

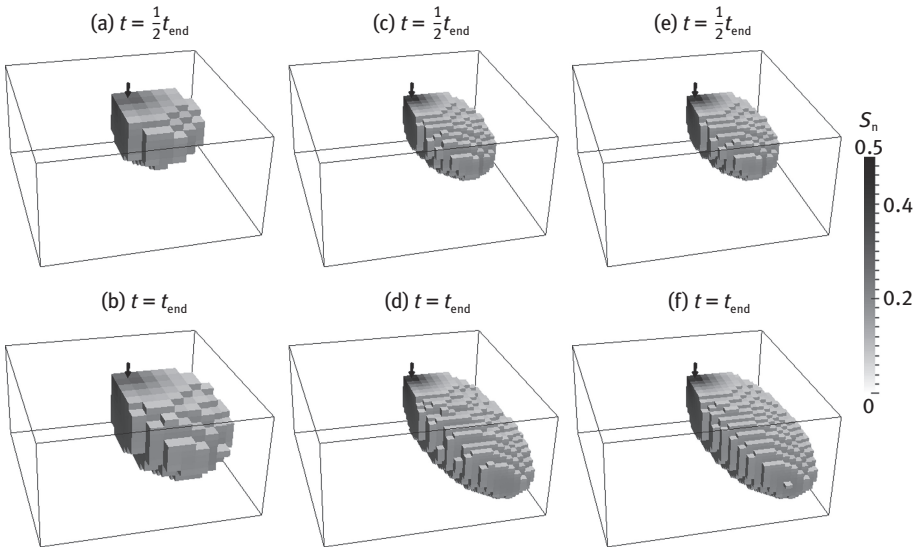


Figure 2.32: DNAPL infiltration case 2: Comparison of the results using a locally refined grid (c) and (d), a coarse structured grid (a) and (b), and a fine structured grid (e) and (f).

tom. The DNAPL distribution calculated by the L-model also flows toward the bottom of the domain but following the diagonal direction given by the off-diagonal entries of the anisotropic permeability tensor. Obviously, the TPFA cannot be used to validate the adaptive L-method for this case. Thus, the results of the adaptive model are compared to a reference solution using the L-method calculated on a structured grid of $32 \times 32 \times 32$ cells, which have the same size as the finest cells of the adapted grid. Additionally, a coarser structured grid of $16 \times 16 \times 16$ cells is used, whose number of degrees of freedom has the order of the averaged number of degrees of freedom of the adapted grid. Figure 2.32 clearly shows that the adaptive scheme obtains the accuracy of the fine structured grid which cannot be achieved by the coarser structured grid of a similar size.

Two grids of the adaptive L-model for case 2 at $t = \frac{1}{2}t_{\text{end}}$ and $t = t_{\text{end}}$ are shown in Figure 2.33. They clearly demonstrate the potential of grid adaptive methods with respect to efficiency. Especially, when large parts of a model domain are not affected by moving fluid fronts, the local grid refinement and coarsening can provide a fine resolution of the fronts while still having feasible grid sizes. This increase of efficiency also allows to use more complex methods like MPFA methods for realistic scenarios where they otherwise could be too expensive.

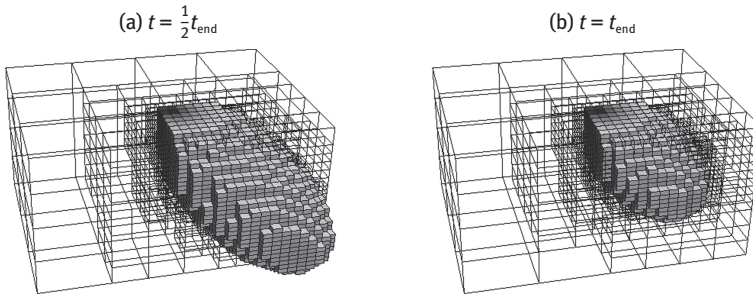


Figure 2.33: Locally adapted grids of the MPFA model for DNAPL case 2 at different simulation times.

5.5 Refinement and coarsening indicator

The quality and applicability of an adaptive method is highly affected by the criteria used for refinement and coarsening. In all our examples, the following local-gradient-based criterion is used:

$$\text{refine} = \begin{cases} \text{true}, & \text{if } \Delta S_{ii} \geq E_{\text{refine}} \\ \text{false}, & \text{else} \end{cases}, \quad (2.26)$$

$$\text{coarsen} = \begin{cases} \text{true}, & \text{if } \Delta S_{ii} < E_{\text{coarsen}} \\ \text{false}, & \text{else} \end{cases}. \quad (2.27)$$

Here, index i is the cell index and ΔS_{ii} is defined as

$$\Delta S_{ii} = \frac{\max(\Delta S_{ij})}{\Delta S_{\max}}, \quad (2.28)$$

where ΔS_{ij} is the saturation difference between cell i and a neighboring cell j and ΔS_{\max} is the global maximum of ΔS_{ij} used for normalization. Further, the refinement threshold E_{refine} is defined as

$$E_{\text{refine}} = \varepsilon_{\text{refine}} \frac{\Delta S_{\max}}{S_{\max} - S_{\min}}, \quad (2.29)$$

where $\varepsilon_{\text{refine}}$ is a threshold value which has to be set (usually between 0 and 1) to control the refinement, and S_{\max} and S_{\min} are the global maximum and minimum, respectively, of the saturation. Similarly, E_{coarsen} is defined as

$$E_{\text{coarsen}} = \varepsilon_{\text{coarsen}} \frac{\Delta S_{\max}}{S_{\max} - S_{\min}}, \quad (2.30)$$

where $\varepsilon_{\text{coarsen}} \leq \varepsilon_{\text{refine}}$ is the threshold value to control the coarsening (usually between 0 and 1). In case of a pure shock front (e.g. if f_α are linear functions) $\Delta S_{\max} = S_{\max} - S_{\min}$ and the adaption behavior is directly controlled by $\varepsilon_{\text{refine}}$ and $\varepsilon_{\text{coarsen}}$. In

all other cases $\varepsilon_{\text{refine}}$ and $\varepsilon_{\text{coarsen}}$ are additionally weighted to account for the fluid distribution. Experience has shown that values of $\varepsilon_{\text{refine}} = 0.5, \dots, 0.9$ and $\varepsilon_{\text{coarsen}} = 0.01, \dots, 0.5$ usually lead to robust adaption behavior. For the DNAPL infiltration examples we additionally force the grid to be refined at the area of the DNAPL inflow to correctly resolve the boundary condition.

6 Summary and conclusions

We have generalized the well-known MPFA L-method in 3D for single and two-phase flow systems to meshes with hanging nodes and applied these pressure-based locally conservative schemes to realistic porous media flow scenarios. A simplified boundary treatment is proposed based on the combination of TPFA techniques and suitable weighting factors. This method is quite flexible and easily applicable to more complex boundary configurations and adaptively refined grids. We further show how the L-method has to be modified in the presence of hanging nodes which appear through nonconforming grid refinement. As shown by our numerical results, the standard L-selection criterion can fail in the case of meshes with highly skewed elements. This observation motivates the introduction of a new selection criterion.

First, the L-scheme has been extensively tested for the elliptic one-phase flow pressure equation. The numerical convergence has been investigated by means of benchmark test problems designed for the FVCA6 conference. Additionally to the given exact solution, the L-method has been compared to the TPFA and the MFD method. The L-method is able to solve both benchmark problems on all grids with sufficient accuracy. The robustness of the method is closely related to the choice of the L-stencil and thus to the L-selection criterion. In most cases both tested criteria lead to robust L-stencils. However, in case of strong non-K-orthogonality which appears at regions of large skewness only the newly proposed criterion could obtain the correct solution for benchmark test 1. As expected, the MPFA is superior to the TPFA in case of non-K-orthogonal grids. Regarding the convergence order, the MFD method shows advantages compared to the L-method. For benchmark test 3 both methods show a $\mathcal{O}(h^2)$ convergence of pressure and normal velocity, but for test 1 the MFD method converges with $\mathcal{O}(h^2)$, while the L-method converges only with $\mathcal{O}(h^1)$. The impact of the simplified boundary treatment can be neglected in many cases, however not in the situation of the random mesh with the nonplanar surface which is used for test 3. Considering more realistic applications, for example in the field of reservoir simulation, such complexity at the boundaries usually does not occur. Additionally, important processes often take place somewhere in the domain and not at the boundaries. Therefore, in most application-relevant settings the simplified boundary treatment can be justified.

Second, we have extended the 3D MPFA L-model to incompressible, isothermal, immiscible two-phase flow. In this case, a parabolic phase transport equation is

weakly coupled to the elliptic two-phase pressure equation, leading to additional requirements for the numerical scheme. It has to be locally mass conservative and be able to account for discontinuous shock fronts as well as for diffusive fronts in capillary-pressure-dominated domains. An additional challenge is the treatment of material interfaces, e.g. between areas of different entry pressures. While there exists a variety of alternative methods like MFD that perform very well for the pressure equation without capillary effects, only a few successful efforts have been undertaken up to now that can handle more complex settings. We have tested the MPFA L-method on two well-known benchmark problems for two-phase flow using unstructured, non-K-orthogonal grids. In these tests, the TPFA fails as expected from the theory, while the MPFA L-method approximates the correct solution very well for both, the advection-dominated as well as the capillary-diffusion-dominated case. Two more tests demonstrate the applicability of the L-model to realistic problems like a DNAPL infiltration scenario. In the first case, the L-method is validated for the case of gravity-dominated flow including heterogeneities. Comparing the TPFA and the MPFA, both models show similar results and account for the heterogeneity as well as they satisfy the capillary-pressure interface condition. However, due to the larger flux stencil the L-method is superior in modeling the sharp changes in direction of the streamlines due to blocking effects at the heterogeneous interfaces. In the second case, the advantage of the L-method in case of an anisotropic porous medium leading to a non-K-orthogonal grid is obvious.

Realistic two-phase flow scenarios in porous media require a numerical model which is flexible with regard to complex geometry of the domain and the domain boundaries, which is able to account for important two-phase flow specific features, and which is efficient enough to run simulations in reasonable time. We have demonstrated that the MPFA L-model can satisfy these requirements by combining it with the flexibility of TPFA along the boundary and by using locally adaptive grids.

References

- [1] J. E. Aarnes, S. Krogstad, and K.-A. Lie, Multiscale mixed/mimetic methods on corner-point grids, *Computational geosciences* 12 (2008), 297–315.
- [2] I. Aavatsmark, An introduction to multipoint flux approximations for quadrilateral grids, *Comput. Geosci.* 6 (2002), 405–432.
- [3] I. Aavatsmark, Interpretation of a two-point flux stencil for skew parallelogram grids, *Comput. Geosci.* 11 (2007), 199–206.
- [4] I. Aavatsmark, T. Barkve, Ø. Bøe, and T. Mannseth, Discretization on non-orthogonal curvilinear grids for multi-phase flow, in: *Proceedings of 4th European Conference on the Mathematics of Oil Recovery*, Røros, Norway, 1994.
- [5] I. Aavatsmark, T. Barkve, and T. Mannseth, Control volume discretization methods for 3D quadrilateral grids in inhomogeneous, anisotropic reservoirs, *SPE J.* 3 (1998), 146–154.
- [6] I. Aavatsmark and G. T. Eigestad, Numerical convergence of the MPFA O-method and U-method for general quadrilateral grids, *Internat. J. Numer. Methods Fluids* 51 (2006), 939–961.

- [7] I. Aavatsmark, G. T. Eigestad, and R. A. Klausen, *Numerical convergence of the MPFA O-method for general quadrilateral grids in two and three dimensions*, Compatible spatial discretizations, Vol. 142, IMA Vol. Math. Appl. (D. N. Arnold, P. B. Bochev, R. B. Lehoucq, R. A. Nicolaides, and M. Shashkov, eds.), Springer, New York, 2006, pp. 1–21.
- [8] I. Aavatsmark, G. T. Eigestad, R. A. Klausen, M. F. Wheeler, and I. Yotov, Convergence of a symmetric MPFA method on quadrilateral grids, *Comput. Geosci.* 11 (2007), 333–345.
- [9] I. Aavatsmark, G. T. Eigestad, B. T. Mallison, and J. M. Nordbotten, A compact multipoint flux approximation method with improved robustness, *Numer. Methods Partial Differential Equations* 24 (2008), 1329–1360.
- [10] I. Aavatsmark, Eigestad, G. T., B.-O. Heimsund, B. T. Mallison, J. M. Nordbotten, and E. Øian, A new finite volume approach to efficient discretization on challenging grids, in: *Proceedings of the SPE Reservoir Simulation Symposium*, Houston, Texas, 2007, SPE 106435.
- [11] L. Agélas and R. Masson, Convergence of the finite volume MPFA O scheme for heterogeneous anisotropic diffusion problems on general meshes, *C. R. Math.* 346 (2008), 1007–1012.
- [12] K. Aziz and A. Settari, *Petroleum reservoir simulation*, Elsevier Applied Science, 1979.
- [13] P. Bastian, M. Blatt, A. Dedner, C. Engwer, R. Klöfkorn, R. Kornhuber, M. Ohlberger, and O. Sander, A generic grid interface for parallel and adaptive scientific computing. Part II: implementation and tests in DUNE, *Computing* 82 (2008), 121–138.
- [14] F. Brezzi, K. Lipnikov, and V. Simoncini, A family of mimetic finite difference methods on polygonal and polyhedral meshes, *Mathematical Models and Methods in Applied Science* 15 (2005), 1533–1551.
- [15] S. E. Buckley and M. C. Leverett, Mechanisms of fluid displacement in sand, *Petroleum Transactions, AIME* 146 (1942), 107–116.
- [16] Y. Cao, R. Helmig, and B. I. Wohlmuth, Geometrical interpretation of the multi-point flux approximation L-method, *Internat. J. Numer. Methods Fluids* 60 (2009), 1173–1199.
- [17] Y. Cao, R. Helmig, and B. I. Wohlmuth, Convergence of the multipoint flux approximation L-method for homogeneous media on uniform grids, *Numer. Methods Partial Differential Equations* 27 (2011), 329–350.
- [18] Q.-Y. Chen, J. Wan, Y. Yang, and R. T. Mifflin, Enriched multi-point flux approximation for general grids, *J. Comput. Phys.* 227 (2008), 1701–1721.
- [19] K H Coats, Impes stability: Selection of stable timesteps, *SPE Journal* 8 (2003), 181–187.
- [20] M. G. Edwards, Unstructured, control-volume distributed, full-tensor finite-volume schemes with flow based grids, *Comput. Geosci.* 6 (2002), 433–452.
- [21] M. G. Edwards and C. F. Rogers, A flux continuous scheme for the full tensor pressure equation, in: *Proceedings of 4th European Conference on the Mathematics of Oil Recovery*, Røros, Norway, 1994.
- [22] M. G. Edwards and H. Zheng, A quasi-positive family of continuous Darcy-flux finite volume schemes with full pressure support, *J. Comput. Phys.* 227 (2008), 9333–9364.
- [23] G. T. Eigestad and R. A. Klausen, On the convergence of the multi-point flux approximation O-method: Numerical experiments for discontinuous permeability, *Numer. Methods Partial Differential Equations* 21 (2005), 1079–1098.
- [24] B. Flemisch, M. Darcis, K. Erbertseder, B. Faigle, A. Lauser, K. Mosthaf, S. Müthing, P. Nuske, A. Tatomir, M. Wolff, and R. Helmig, DuMux: DUNE for multi-{phase, component, scale, physics, ...} flow and transport in porous media, *Advances in Water Resources* 34 (2011), 1102–1112.
- [25] J. Fořt, J. Fürst, J. Halama, R. Herbin, and F Hubert (eds.), *Finite volumes for complex applications VI Problems & perspectives*, Proceedings in mathematics 4, Springer, 2011.

- [26] D. Gunasekera, P. Childs, J. Herring, and J. Cox, A multi-point flux discretization scheme for general polyhedral grids, in: *Proceedings of the SPE International Oil and Gas Conference and Exhibition in China*, Beijing, China, 1998, SPE 48855.
- [27] R. Helmig, *Multiphase flow and transport processes in the subsurface: a contribution to the modeling of hydrosystems*, Springer, Berlin, 1997.
- [28] R. Helmig and R. Huber, Comparison of Galerkin-type discretization techniques for two-phase flow in heterogeneous porous media, *Advances in Water Resources* 21 (1998), 697 – 711.
- [29] Z. E. Helnemann, C. W. Brand, M. Munka, and Y. M. Chen, Modeling reservoir geometry with irregular grids, *SPE Reservoir Engineering* 6 (1991), 225–232.
- [30] H. Hoteit and A. Firoozabadi, Numerical modeling of two-phase flow in heterogeneous permeable media with different capillarity pressures, *Advances in water resources* 31 (2008), 56–73.
- [31] D. S. Kershaw, Differencing of the diffusion equation in Lagrangian hydrodynamic codes, *J. Comput. Phys.* 39 (1981), 375–395.
- [32] R. A. Klausen and A. F. Stephansen, Convergence of the MPFA O-method on general grids, *Numer. Methods Partial Differential Equations* submitted.
- [33] R. A. Klausen and R. Winther, Robust convergence of multi point flux approximation on rough grids, *Numer. Math.* 104 (2006), 317–337.
- [34] S. H. Lee, H. A. Tchelepi, P. Jenny, and L. J. DeChant, Implementation of a flux-continuous finite-difference method for stratigraphic, hexahedron grids, *SPE J.* 7 (2002), 267–277.
- [35] D. B. McWhorter and D. K. Sunada, Exact integral solutions for two-phase flow, *Water Resour. Res* 26 (1990), 399–413.
- [36] S. Mundal, D. A. Di Pietro, and I. Aavatsmark, Compact-stencil MPFA method for heterogeneous highly anisotropic second-order elliptic problems, in: *Finite Volumes for Complex Applications V (Problems & Perspectives)* (R. Eymard and J. M. Hérard, eds.), pp. 905–918, Wiley, 2008.
- [37] J. M. Nordbotten and I. Aavatsmark, Monotonicity conditions for control volume methods on uniform parallelogram grids in homogeneous media, *Comput. Geosci.* 9 (2005), 61–72.
- [38] J. M. Nordbotten, I. Aavatsmark, and G. T. Eigestad, Monotonicity of control volume methods, *Numer. Math.* 106 (2007), 255–288.
- [39] J. M. Nordbotten and G. T. Eigestad, Discretization on quadrilateral grids with improved monotonicity properties, *J. Comput. Phys.* 203 (2005), 744–760.
- [40] M. Pal and M. G. Edwards, Quasi-monotonic continuous Darcy-flux approximation for general 3-D grids of any element type, in: *Proceedings of the SPE Reservoir Simulation Symposium*, Houston, 2007, SPE 106486.
- [41] M. Pal, M. G. Edwards, and A. R. Lamb, Convergence study of a family of flux-continuous finite-volume schemes for the general tensor pressure equation, *Internat. J. Numer. Methods Fluids* 51 (2006), 1177–1203.
- [42] A. Scheidegger, *The physics of flow through porous media*, 3d ed, University of Toronto Press, 1974.
- [43] O. Schenk, M. Bollhoefer, and R. Roemer, On large-scale diagonalization techniques for the Anderson model of localization, *SIAM Review* 50 (2008), 91–112.
- [44] O. Schenk, A. Waechter, and M. Hagemann, Matching-based preprocessing algorithms to the solution of saddle-point problems in large-scale nonconvex interior-point optimization, *Journal of Computational Optimization and Applications* 36 (2007), 321–341.
- [45] Z. Sheng and G. Yuan, A nine point scheme for the approximation of diffusion operators on distorted quadrilateral meshes, *SIAM J. Sci. Comput.* 30 (2008), 1341–1361.
- [46] A. Stephansen, Convergence of the MPFA L-method - strengths and difficulties, in: *Proceedings of 12th European Conference on the Mathematics of Oil Recovery*, Oxford, UK, 2010.

- [47] Martin Vohralík, Equivalence between lowest-order mixed finite element and multi-point finite volume methods on simplicial meshes, *M2AN Math. Model. Numer. Anal.* 40 (2006), 367–391.
- [48] M. F. Wheeler and I. Yotov, A cell-centered finite difference method on quadrilaterals, Compatible spatial discretizations, Vol. 142, IMA Vol. Math. Appl. (D. N. Arnold, P. B. Bochev, R. B. Lehoucq, R. A. Nicolaides, and M. Shashkov, eds.), Springer, New York, 2006, pp. 189–207.
- [49] M. Wolff, B. Flemisch, R. Helmig, and I. Aavatsmark, Treatment of tensorial relative permeabilities with multipoint flux approximation, *International journal of numerical analysis & modeling.* 9 (2012), 725–744.
- [50] X. H. Wu and R. R. Parashkevov, Effect of grid deviation on flow solutions, in: *Proceedings of the SPE Reservoir Simulation Symposium*, Houston, 2005, SPE 92868.

Appendix

In this appendix, the detailed transmissibility matrices $\mathbf{T} = \mathbf{C}\mathbf{A}^{-1}\mathbf{B} + \mathbf{D}$ for the L-stencils (b)–(d) in Figure 2.2 are additionally given for implementation purposes. For the definition of the matrix elements, the reader is referred to Section 2.1.

L-stencil (b)

$$\mathbf{C} = \begin{pmatrix} -\omega_{121} & -\omega_{122} & -\omega_{123} \\ -\omega_{221} & -\omega_{222} & -\omega_{223} \\ -\omega_{321} & -\omega_{322} & -\omega_{323} \end{pmatrix}, \quad \mathbf{D} = \begin{pmatrix} 0 & \omega_{121} + \omega_{122} + \omega_{123} & 0 & 0 \\ 0 & \omega_{221} + \omega_{222} + \omega_{223} & 0 & 0 \\ 0 & \omega_{321} + \omega_{322} + \omega_{323} & 0 & 0 \end{pmatrix},$$

$$\mathbf{A} = \begin{pmatrix} \omega_{121} - \omega_{112} - & \omega_{122} - \omega_{111}r_{221} - & \omega_{123} - \omega_{111}r_{231} - \\ \omega_{111}r_{211} - \omega_{113}r_{212} & \omega_{113}r_{222} & \omega_{113}r_{232} \\ \omega_{221} - \omega_{242}r_{211} - & \omega_{222} - \omega_{241} - & \omega_{223} - \omega_{242}r_{231} - \\ \omega_{243}r_{213} & \omega_{242}r_{221} - \omega_{243}r_{223} & \omega_{243}r_{233} \\ \omega_{321} - \omega_{361}r_{213} - & \omega_{322} - \omega_{361}r_{223} - & \omega_{323} - \omega_{363} - \\ \omega_{362}r_{212} & \omega_{362}r_{222} & \omega_{361}r_{233} - \omega_{362}r_{232} \end{pmatrix},$$

$$\mathbf{B} = \begin{pmatrix} -(\omega_{111} + & \omega_{121} + \omega_{122} + \omega_{123} + & 0 & 0 \\ \omega_{112} + \omega_{113}) & \omega_{111}(1 - r_{211} - r_{221} - r_{231}) + & & \\ & \omega_{113}(1 - r_{212} - r_{222} - r_{232}) & & \\ 0 & \omega_{221} + \omega_{222} + \omega_{223} + & -(\omega_{241} + & 0 \\ & \omega_{242}(1 - r_{211} - r_{221} - r_{231}) + & \omega_{242} + \omega_{243}) & \\ & \omega_{243}(1 - r_{213} - r_{223} - r_{233}) & & \\ 0 & \omega_{321} + \omega_{322} + \omega_{323} + & 0 & -(\omega_{361} + \\ & \omega_{361}(1 - r_{213} - r_{223} - r_{233}) + & & \omega_{362} + \omega_{363}) \\ & \omega_{362}(1 - r_{212} - r_{222} - r_{232}) & & \end{pmatrix}$$

L-stencil (c)

$$\mathbf{C} = \begin{pmatrix} -\omega_{111} - c\omega_{113}r_{231}r_{112} & -c\omega_{113}r_{221} & -\omega_{112} - c\omega_{113}r_{231}r_{122} \\ c\omega_{113}r_{211} & -\omega_{221} - c\omega_{223}r_{112} & -c\omega_{223}r_{122} \\ -\omega_{221} - c\omega_{223}r_{112} & -\omega_{222} - c\omega_{223}r_{132}r_{221} & -c\omega_{223}r_{122} \\ c\omega_{223}r_{132}r_{211} & c\omega_{311} - c\omega_{313}r_{231}r_{112} & -\omega_{312} - c\omega_{313}r_{231}r_{122} \\ -\omega_{311} - c\omega_{313}r_{231}r_{112} & c\omega_{313}r_{211} & \end{pmatrix},$$

$$\mathbf{D} = \begin{pmatrix} c\omega_{113}r_{231}(r_{112} + r_{122} + r_{132} - 1) & c\omega_{113}(r_{211} + r_{221} + r_{231} - 1) & 0 & 0 \\ +\omega_{111} + \omega_{112} + \omega_{113} & & & \\ c\omega_{223}(r_{112} + r_{122} + r_{132} - 1) & \omega_{221} + \omega_{222} + \omega_{223} + c\omega_{223}r_{132}(r_{211} + r_{221} + r_{231} - 1) & 0 & 0 \\ c\omega_{313}r_{231}(r_{112} + r_{122} + r_{132} - 1) & c\omega_{313}(r_{211} + r_{221} + r_{231} - 1) & 0 & 0 \\ +\omega_{311} + \omega_{312} + \omega_{313} & & & \end{pmatrix},$$

$$\mathbf{A} = \begin{pmatrix} \omega_{111} - \omega_{121} + c\omega_{113}(r_{231}r_{112} + r_{211}) & c\omega_{113}r_{221} - \omega_{122} & \omega_{112} + c\omega_{113}r_{231}r_{122} & -c\omega_{123}r_{122} \\ c\omega_{113}(r_{231}r_{112} + r_{211}) & -c\omega_{123}r_{132}r_{221} & & \\ -c\omega_{123}(r_{112} + r_{132}r_{211}) & & & \\ \omega_{221} - \omega_{243}r_{214} + c(\omega_{223} - \omega_{243}r_{234})(r_{112} + r_{132}r_{211}) & \omega_{222} - \omega_{243}r_{224} - \omega_{241} + c(\omega_{223} - \omega_{243}r_{234})r_{132}r_{221} & cr_{122}(\omega_{223} - \omega_{243}r_{234}) & -\omega_{242}r_{231} \\ \omega_{243}r_{234})(r_{112} + r_{132}r_{211}) & c(\omega_{223} - \omega_{243}r_{234})r_{132}r_{221} & & \\ -c\omega_{242}(r_{231}r_{112} + r_{211}) & -c\omega_{242}r_{221} & & \\ \omega_{311} - \omega_{353}r_{113} + c(\omega_{313} - \omega_{353}r_{133})(r_{231}r_{112} + r_{211}) & cr_{221}(\omega_{313} - \omega_{353}r_{133}) & \omega_{312} - \omega_{351} - \omega_{353}r_{123} + c(\omega_{313} - \omega_{353}r_{133})r_{231}r_{122} & -c\omega_{352}r_{122} \\ \omega_{353}r_{133})(r_{231}r_{112} + r_{211}) & -\omega_{352}r_{132} & & \\ -c\omega_{352}(r_{112} + r_{132}r_{211}) & & & \end{pmatrix},$$

$$\mathbf{B} = \begin{pmatrix} c(\omega_{113}r_{231} - \omega_{123}) \cdot (r_{112} + r_{122} + r_{132} - 1) + \omega_{111} + \omega_{112} + \omega_{113} & c(\omega_{113} - \omega_{123}r_{132}) \cdot (r_{211} + r_{221} + r_{231} - 1) - (\omega_{121} + \omega_{122} + \omega_{123}) & 0 & 0 \\ & & & \\ c(r_{112} + r_{122} + r_{132} - 1) \cdot (\omega_{223} - \omega_{243}r_{234} - \omega_{242}r_{231}) & \omega_{221} + \omega_{222} + \omega_{223} - \omega_{243}(r_{214} + r_{224} + r_{234} - 1) + c(r_{211} + r_{221} + r_{231} - 1) \cdot (\omega_{223}r_{132} - \omega_{243}r_{234}r_{132} - \omega_{242}) & -(\omega_{241} + \omega_{242} + \omega_{243}) & 0 \\ (\omega_{313}r_{231} - \omega_{353}r_{133}r_{231} - \omega_{352}) + \omega_{311} + \omega_{312} + \omega_{313} - \omega_{353}(r_{113} + r_{123} + r_{133} - 1) & c(r_{211} + r_{221} + r_{231} - 1) \cdot (\omega_{313} - \omega_{353}r_{133} - \omega_{352}r_{132}) & 0 & -(\omega_{351} + \omega_{352} + \omega_{353}) \end{pmatrix}.$$

Here, the constant $c = \frac{1}{1 - r_{231}r_{132}}$.

L-stencil (d)

$$\mathbf{C} = \begin{pmatrix} -\omega_{111} - c\omega_{113}r_{212} - & -\omega_{112} - c\omega_{113}r_{232}r_{121} & -c\omega_{113}r_{222} \\ c\omega_{113}r_{232}r_{111} & & \\ -\omega_{211} - c\omega_{213}r_{212} - & -\omega_{212} - c\omega_{213}r_{232}r_{121} & -c\omega_{213}r_{222} \\ c\omega_{213}r_{232}r_{111} & & \\ -\omega_{321} - c\omega_{323}r_{111} - & -c\omega_{323}r_{121} & -\omega_{322} - c\omega_{323}r_{131}r_{222} \\ c\omega_{323}r_{131}r_{212} & & \end{pmatrix},$$

$$\mathbf{D} = \begin{pmatrix} c\omega_{113}r_{232}(r_{111} + r_{121} + r_{131} - 1) & c\omega_{113}(r_{212} + r_{222} + r_{232} - 1) & 0 & 0 \\ +\omega_{111} + \omega_{112} + \omega_{113} & & & \\ c\omega_{213}r_{232}(r_{111} + r_{121} + r_{131} - 1) & c\omega_{213}(r_{212} + r_{222} + r_{232} - 1) & 0 & 0 \\ +\omega_{211} + \omega_{212} + \omega_{213} & & & \\ c\omega_{323}(r_{111} + r_{121} + r_{131} - 1) & c\omega_{323}r_{131}(r_{212} + r_{222} + r_{232} - 1) & 0 & 0 \\ +\omega_{321} + \omega_{322} + \omega_{323} & & & \end{pmatrix},$$

$$\mathbf{A} = \begin{pmatrix} \omega_{111} - \omega_{121} + & \omega_{112} + c\omega_{113}r_{232}r_{121} & c\omega_{113}r_{222} - \omega_{122} - \\ c\omega_{113}(r_{212} + r_{232}r_{111}) - & -c\omega_{123}r_{121} & c\omega_{123}r_{131}r_{222} \\ c\omega_{123}(r_{111} + r_{131}r_{212}) & & \\ \omega_{211} - \omega_{233}r_{114} + & \omega_{212} - \omega_{231} - \omega_{233}r_{124} + & c\omega_{222}(\omega_{213} - \\ c(\omega_{213} - \omega_{233}r_{134}) \cdot & c(\omega_{213} - \omega_{233}r_{134})r_{232}r_{121} & \omega_{233}r_{134} - \omega_{232}r_{131}) \\ (r_{212} + r_{232}r_{111}) - & -c\omega_{232}r_{121} & \\ c\omega_{232}(r_{111} + r_{131}r_{212}) & & \\ \omega_{321} - \omega_{363}r_{213} + & c\omega_{121}(\omega_{323} - \omega_{363}r_{233} & \omega_{322} - \omega_{361} - \omega_{363}r_{223} + \\ c(\omega_{323} - \omega_{363}r_{233}) \cdot & -\omega_{362}r_{232}) & c(\omega_{323} - \omega_{363}r_{233})r_{131}r_{222} \\ (r_{111} + r_{131}r_{212}) - & & -c\omega_{362}r_{222} \\ c\omega_{362}(r_{212} + r_{232}r_{111}) & & \end{pmatrix},$$

$$\mathbf{B} = \begin{pmatrix} c(\omega_{113}r_{232} - \omega_{123}) \cdot & c(\omega_{113} - \omega_{123}r_{131}) \cdot & & \\ (r_{111} + r_{121} + r_{131} - 1) & (r_{212} + r_{222} + r_{232} - 1) & 0 & 0 \\ +\omega_{111} + \omega_{112} + \omega_{113} & -(r_{121} + \omega_{122} + \omega_{123}) & & \\ \omega_{211} + \omega_{212} + \omega_{213} - & & & \\ \omega_{233}(r_{114} + r_{124} + r_{134} - 1) + & c(r_{212} + r_{222} + r_{232} - 1) \cdot & -(\omega_{231} + & 0 \\ c(r_{111} + r_{121} + r_{131} - 1) \cdot & (\omega_{213} - \omega_{233}r_{134} - & \omega_{232} + \omega_{233}) & \\ (\omega_{213}r_{232} - \omega_{233}r_{134}r_{232} & \omega_{232}r_{131}) & & \\ -\omega_{232}) & & & \\ & \omega_{321} + \omega_{322} + \omega_{323} - & & \\ & c(r_{111} + r_{121} + r_{131} - 1) \cdot & -(\omega_{361} + & 0 \\ (\omega_{323} - \omega_{363}r_{233} - \omega_{362}r_{232}) & (\omega_{323}r_{131} - \omega_{363}r_{233}r_{131} & \omega_{362} + \omega_{363}) & \\ -\omega_{362}) & -\omega_{362}) & & \end{pmatrix}.$$

Here, the constant $c = \frac{1}{1 - r_{232}r_{131}}$.